Carbonate alteration of ophiolitic rocks in the Arabian-Nubian Shield of Egypt: Sources and compositions of the carbonating fluid and implications for the formation of Au deposits

Journal:	*International Geology Review*
Manuscript ID	TIGR-2016-0025.R2
Manuscript Type:	Data Article
Date Submitted by the Author:	13-Aug-2016
Complete List of Authors:	Boskabadi, Arman; The University of Texas at Dallas, Department of Geosciences, ROC 21; Stockholms Universitet, Department of Geological Sciences Pitcairn, Iain; Stockholms Universitet, Department of Geological Sciences Broman, Curt; Stockholms Universitet, Department of Geological Sciences Boyce, Adrian; Scottish Universities Environmental Research Centre Teagle , Damon; National Oceanography Center, University of Southampton Cooper, Matthew; National Oceanography Center, University of Southampton Azer, Mokhles; National Research centre, Geological Sciences Stern, Robert; U Texas at Dallas, Mohamed, Fathy; Alexandria University Faculty of Science, Geology department MAJKA, JAROSLAW ; Uppsala University
Keywords:	Arabian-Nubian Shield, serpentinite, Listvenite, Carbonation, Gold, Fluid-mobile elements, Stable isotopes, Sr isotopes

Carbonate alteration of ophiolitic rocks in the Arabian-Nubian Shield of Egypt: Sources and compositions of the carbonating fluid and implications for the formation of Au deposits

ARMAN BOSKABADI[1, 2], IAIN K. PITCAIRN[2], CURT BROMAN[2], ADRIAN BOYCE[3], DAMON A. H. TEAGLE[4], MATTHEW J. COOPER[4], MOKHLES K. AZER[5], ROBERT J. STERN[1], FATHY H. MOHAMED[6], JAROSLAW MAJKA[7,8]

[1] Geosciences Department, University of Texas at Dallas, Texas, USA
[2]Department of Geological Sciences, Stockholm University, Stockholm, Sweden
[3] Scottish Universities Environmental Research Centre, East Kilbride, UK
[4] National Oceanography Centre Southampton, University of Southampton, SO14 3ZH, UK.
[5] Geology Department, National Research Centre, Cairo, Egypt
[6] Geology Department, Faculty of science, Alexandria University, Alexandria, Egypt
[7] Department of Earth Sciences, Uppsala University, Uppsala, Sweden
[8] Faculty of Geology, Geophysics and Environmental Protection, AGH – University of Science and Technology, Kraków, Poland

Corresponding author details:
Arman Boskabadi
The University of Texas at Dallas
Department of Geosciences, ROC 21
800 West Campbell Road
Richardson, TX 75080-3021
Email: arman.boskabadi@utdallas.edu

Abstract

Ultramafic portions of ophiolitic fragments in the Arabian-Nubian Shield (ANS) show pervasive carbonate alteration forming various degrees of carbonated serpentinites and listvenitic rocks. Despite the extent of the alteration, little is known about the processes that caused it, the source of the CO_2, or the conditions of alteration. This study investigates the mineralogy, stable (O, C) and radiogenic (Sr) isotope composition, and geochemistry of suites of variably carbonate altered ultramafics from the Meatiq area of the Central Eastern Desert (CED) of Egypt. The samples investigated include least-altered lizardite (Lz) serpentinites, antigorite (Atg) serpentinites, and listvenitic rocks with associated carbonate and quartz veins. The C, O and Sr isotopes of the vein samples cluster between -8.1‰ to -6.8‰ for $\delta^{13}C$, +6.4‰ to +10.5‰ for $\delta^{18}O$, and $^{87}Sr/^{86}Sr$ of 0.7028 to 0.70344, and plot within the depleted mantle compositional field. The serpentinites isotopic compositions plot on a mixing trend between the depleted-mantle and sedimentary carbonate fields. The carbonate veins contain abundant carbonic (CO_2±CH_4±N_2) and aqueous-carbonic (H_2O-NaCl-CO_2±CH_4±N_2) low salinity fluid, with trapping conditions of 270°C to 300°C and 0.7 to 1.1 kbar. The serpentinites are enriched in Au, As, S and other fluid-mobile elements relative to primitive and depleted mantle. The extensively carbonated Atg-serpentinites contain significantly lower concentrations of these elements than the Lz-serpentinites suggesting that they were depleted during carbonate alteration. Fluid inclusion and stable isotope compositions of Au deposits in the CED are similar to those from the carbonate veins investigated in the study and we suggest that carbonation of ANS ophiolitic rocks due to influx of mantle-derived CO_2-bearing fluids caused break down of Au-bearing minerals such as pentlandite, releasing Au and S to the hydrothermal fluids that later formed the Au-deposits. This is the first time that Au has been observed to be remobilized from rocks during the lizardite-antigorite transition.

Keywords: Arabian-Nubian Shield, serpentinite, Listvenite, Carbonation, Gold, Fluid-mobile elements, Stable isotopes, Sr isotopes

1. Introduction

Carbonation of mafic and ultramafic rocks is an important geological process with implications that include carbon sequestration (Lackner et al. 1995; Selfritz 1990; Kelemen and Matter 2008), the carbon cycle and fluxing of CO_2 to the Earth's atmosphere (Kerrick and Caldiera 1998; Lasaga et al. 2001; Skelton 2011), and formation of ore deposits (Barnes et al. 1973; Groves et al. 1998; Phillips and Evans 2004). Carbonation occurs when susceptible rocks in the crust and mantle interact with CO_2-rich fluids resulting in alteration and precipitation of carbonate and other minerals. Mafic and ultramafic rocks are particularly prone to carbonation due to abundant olivine [$(Mg,Fe)_2SiO_4$] and pyroxene

[$(Ca,Mg,Fe)_2Si_2O_6$], which react with H_2O and CO_2 to form hydrous silicates such as serpentine, Fe-oxides (magnetite) and carbonates (Kelemen and Matter 2008). Carbonation of mafic rocks has been used to calculate fluxes of CO_2 to the Earth's atmosphere in the geological past (Skelton 2011), and may be linked to formation of Au deposits worldwide (Groves et al. 1998).

Ophiolites of Arabian-Nubian Shield (ANS) are fragments of the Mozambique Oceanic crust generated in a suprasubduction zone setting during Neoproterozoic time (Stern et al. 2004; Azer and Stern 2007). The ophiolites constitute one of the most distinctive rock sequences among ANS basement rocks (Fig. 1). The ophiolitic rocks are commonly altered due in part to interaction with migrating carbonate-rich solutions (Stern and Gwinn 1990). Carbonation of the ophiolite units is extensive and indicates a large flux of CO_2-bearing fluid. However there have been few investigations into the sources and composition of carbonating fluids, or the conditions at which this alteration occurred. The carbonation has been focused along faults and shear zones and has resulted in formation of variably foliated talc-rich rocks previously referred to as 'talc-carbonate schists', 'Barramiya rocks', 'listvenite-like rocks' (Azer 2013) or 'talc-rich rocks' (Stern et al. 2004; Ali-Bik et al. 2012).

The ophiolitic rocks in some parts of the ANS such as the Central Eastern Desert (CED) of Egypt contain abundant Au deposits (Fig. 1) that have been mined since Pharaonic times (Harraz 2000; Klemm and Klemm 2013). A significant proportion of these deposits occur in or near carbonated ultramafic rocks (Osman 1995; Botros 2002, 2004; Abd El-Rahman et al. 2012; Zoheir and Lehmann 2011). Despite this clear spatial relationship, the genetic relationship between carbonation, deformation and Au deposition remains poorly understood.

This study investigates the sources and compositions of carbonate altered serpentinites in the Meatiq area of the CED. We use stable (C, O) and radiogenic (Sr) isotopes to determine the source of CO_2-rich fluids, and fluid inclusion microthermometry and mineral chemistry to constrain the conditions of alteration. This study also investigates the element mobility that has occurred during the carbonate alteration and discusses the implications of these results for the formation of Au deposits in the CED.

2. Geological Setting

The Arabian- Nubian Shield represents the northern part of East African Orogen (EAO) which formed in Tonian and Cryogenian time accompanying terrane accretion around the Mozambique Ocean (Stern 1994, 2002). The Egyptian segment of the ANS is exposed in the Eastern Desert (ED) and can be subdivided into four main lithotectonic units: (i) a lower unit "infrastructure" composed of gneiss and deformed granitoids, (ii) a structurally overlying "suprastructure" composed of metamorphosed ophiolitic and island arc assemblages, (iii) a sequence of non-metamorphosed to weakly metamorphosed and deformed volcanic (Dokhan Volcanics) and sedimentary rocks (Hammamat Group) that unconformably overlie the suprastructure in places, and (iv) post-orogenic granitic plutons that commonly intrude the other units (Andresen et al. 2009, 2010). Over 30 different locations of ophiolites have been mapped in the Egyptian segment of the ANS. (Fig. 1; Stern et al. 2004). These consist of

tectonically disrupted fragments of mantle serpentinized ultramafic rocks and crustal gabbro, sheeted dykes and pillow basalts (Stern et al. 2004). CED ophiolitic rocks are strongly deformed and metamorphosed to conditions of lower greenschist and amphibolite facies (Johnson et al. 2004, Stern et al. 2004). Radiometric ages of ANS ophiolites range between 880 and 740 Ma (Ries et al. 1983; Kröner 1985; Kröner et al. 1992, 1994; Stern 1994; Loizenbauer et al. 2001), with two age maxima from about 850 to 780 Ma and from 750 to 700 Ma (Stern 1994).

[Insert figure 1 near here]

The study area is known as Meatiq dome which is located about 40 km west of the Red Sea (Fig. 1 and 2). The Meatiq dome is a large, c. 500 km^2 quartzofeldspathic gneiss complex surrounded by low-grade ophiolitic melange (Andresen et al. 2010). The eastern and western dome margins are bounded by sinistral strike-slip shear zones which belong to the Najd Fault System whereas the northern and southern margins are defined by prominent normal faults (Fig. 2, Wallbrecher et al. 1993). Um Ba'anib Orthogneiss that comprises the core of the Meatiq dome consists of coarse-grained, foliated orthogneisses that become gradually more mylonitized and fine-grained at shallower levels, forming a garnet-bearing mylonitic carapace (Andresen et al. 2009). The Um Ba'anib orthogneiss and the upper metasediments are often considered to be "infrastructure" (Habib et al. 1985; Neumayr et al. 1996, 1998). The protolith age of the Um Ba'anib Orthogneiss is 631 Ma, whereas the undeformed Arieki granite intruded the succession at 590 Ma (Andresen et al. 2009).

A variably mylonitized and metamorphosed package of ortho- and paragneisses, overlies the Um Ba'anib Orthogneiss. These are grouped as mylonitized gneisses and called Abu Fananni Thrust Sheet by Habib et al. (1985). A detailed description of the metamorphic evolution of the Abu Fannani Thrust Sheet is given by Neumayr et al. (1996, 1998) and Loizenbauer et al. (2001). The mylonitized paragneisses are intruded in south by the syn-tectonic Abu Ziran diorite which yields a U-Pb zircon and titanite age of 606 Ma (Andresen et al. 2009). The Abu Ziran diorite is generally undeformed, but the western margin of the pluton contains a >50m wide ductile shear zone (Andresen et al. 2009).

The structurally overlying ophiolitic and island arc assemblages are considered to be "suprastructure" (Habib et al. 1985; Neumayr et al. 1996, 1998), Pan-African nappe complex (El-Gaby et al. 1988; Bregar et al. 2002) or eugeoclinal allochthon (Andresen et al. 2009, 2010), and are characterized by greenschist- to lower amphibole facies mineral assemblages (Neumayr et al. 1998). A high-strain zone separates the amphibolite-facies orthogneisses in the core of the high-grade metamorphic domes from the surrounding lower grade ophiolitic rocks (Sturchio et al. 1983; Ries et al. 1983; Habib et al. 1985). Ophiolitic rocks of the Meatiq area comprise mainly serpentinites and their altered products such as listvenitic rocks, metagabbros and metabasalts. Strictly speaking, the term listvenite (also spelled listvanite, listwanite, listwaenite; Kelemen et al. 2011) refers to fuchsite-quartz-carbonate lithologies derived from ultramafic rocks by potassic and carbonate metasomatism (Halls and Zhao 1995). Fuchsite is absent in the samples we studied, and they are also carbonate-poor, and therefore we prefer to use the terms talc-rich and/or listvenitic rocks instead of talc carbonates or listvenites.

The contact of serpentinites with country rocks is highly sheared and deformed with the development of mylonitized metasediments (Loizenbauer et al. 2001). Serpentinites constitute up to 10% of the total area of suprastructure around the gneiss dome and form elongated folded tabular bodies or sheets (Fig. 2). Ophiolitic serpentinites underlie and are intercalated with the metavolcanosedimentary rocks. Andresen et al. (2009) reported a crystallization age of 736.5±1.2 Ma for zircons from an ophiolitic gabbro of the western part of Meatiq (Fawakhir area), which we take to approximate the age of ophiolites in the study area. A detailed age constraints on the evolution of the Neoproterozoic Meatiq dome is given by (Andresen et al. 2009).

A simple interpretation of the structural evolution of the Meatiq dome study area is that ophiolitic suprastructure originally rested roughly horizontally above gneiss infrastructure. Some of the shears in the suprastructure formed during ophiolite emplacement sometime after 736 Ma. High heat flow accompanying syntectonic granitoid emplacement weakened the infrastructure at roughly the same time as the Najd deformation occurred at ~600 Ma. The heating combined with the Najd deformation caused upwelling of the infrastructure forming the Meatiq Dome (Andresen et al. 2009). If this interpretation is approximately true, then study areas A, B, and C are all components of the lower suprastructure, and carbonate alteration occurred at one or more times during this sequence.

[Insert figure 2 near here]

The Fawakhir Au mine (Au = 1.5–29.7 g/ton; Hussein 1990) occurs in the western part of the study area, associated with a 15m wide zone of graphitic schist in the contact of serpentinites, metagabbros and granitoids. It is one of the several Au mines associated with CED ophiolitic rocks that have been extensively worked since Pharaonic and Roman times (Harraz 2000).

3. Sampling

In order to investigate the sources of fluids, the conditions of alteration, and chemical changes during alteration of the ophiolitic fragments in the Meatiq area, a suite of 17 samples of serpentinites, talc-rich rocks and associated quartz and carbonate veins were collected (Table 1). The samples were collected from three main localities with the choice of sample area controlled by the style of serpentinization, the extent of carbonation, and crucially, the availability of fresh, unweathered material. Talc-rich samples in particular are extremely easily weathered, and therefore most of these samples were collected from quarries. Locality A consists of large roadside exposures of serpentinite SW of the Meatiq dome (Fig. 2). The serpentinite outcrops are brownish grey in colour and occur as massive units with brecciation along faults with clearly developed macroscopic mesh texture and cross-cutting chrysotile veinlets in hand specimen scale (Fig. 3a, b). These rocks represent the least altered serpentinites in the study area. Locality B on the NE flank of the dome shows a complex exposure of greenish grey serpentinite and shear zone hosted talc-rich rocks (Fig 3c, 4). The serpentinites from locality B are softer and do not show the chrysotile veinlets seen at locality A. These rocks are heavily sheared in places with yellowish-white to brownish-cream coloured talc-rich rocks occurring in the shear zones (Fig. 3d, e). Veins, nodules and irregular pockets of magnesite and dolomite with quartz occur within the talc-rich bodies (Fig. 3e).

The quartz and carbonate veins generally have a NW-SE trend concordant with the foliation in the talc-rich bodies (Fig. 3e, 4).

The talc-rich rocks are mostly very easily weathered and so despite the excellent exposures in this area, sampling of these rocks was limited. Most samples from locality B were collected from a talc quarry (Fig. 3f, 4). The contacts between the talc-rich rocks and the serpentinite range from gradational to sharp (Fig. 3d), and some talc-rich bodies were observed to have a sharp contact on one side and a gradational contact on the other (Fig. 4).

[Insert figure 3 near here]

Locality C, which occurs SE of locality B, shows a shear zone hosted exposure of talc-rich rocks within serpentinites (Figs. 3g to 3j). The area exhibits the structural controls on listvenitization with the majority of talc-rich bodies showing sharp fault contacts (Figs. 3g, h). These rocks in shear zones experienced intensive mylonitization and are characterized by talcose and schistose fabrics making talc-schists (Fig. 3i). At one area the talc-rich rocks have been partially excavated allowing sampling of relatively fresh rocks. These bodies extend up to several hundred meters in length and are up to 25 meters wide (Fig. 3j).

[Insert figure 4 near here]

4. Analytical methods

SEM

Polished thin-sections of selected serpentinites, talc-rich rocks and carbonate veins were examined with a Philips XL30 FEG environmental scanning electron microscope (ESEM) at Stockholm University, operating at 20kv and equipped with OXFORD energy dispersive analytical X-ray spectrometer. The spectrometer detects elements with atomic number >4 (B and heavier elements).

EPMA

In-situ analyses of Cr-spinels of Lz-serpentinites were carried out using a field emission electron probe microanalyser (FE-EPMA), JXA-8530F JEOL HYPERPROBE at Department of Earth Sciences, Uppsala University, Sweden. Analytical conditions were 15kV accelerating voltage, 10 nA probe current and 1 μm beam diameter, and the raw data were corrected with an PAP routine. Counting time was 10s on peak and 5s on +/- background. Kα spectral lines were measured. Analytical standards were natural and synthetic silicates and oxides. The compositions of chromite are recalculated to cation proportions using the Fe^{3+} calculation scheme of Droop (1987). The results are reported in Supplementary Table.

Gold analyses

Gold analyses were carried out at Stockholm University, using Thermo Xseries 2 ICP-MS following the ultra-low detection limit method described in Pitcairn et al. (2006, 2014). The 3σ method detection limit is 0.033 ppb Au. Analytical precision for Au analyses were controlled through analyses of CANMET reference material TDB1 and USGS reference

materials WMS-1, CH-4. In order to obtain representative Au concentrations in serpentinites, nine hand specimen samples of serpentinite were divided into two groups, and were powdered separately (total of 18 rock powder) using a hardened steel tema. The Au concentrations of these two groups are reported separately in Table 1. Arsenic and antimony analyses were also carried out at Stockholm University, by hydride generation-atomic fluorescence spectrometry (HG-AFS) using a PSA 10.055 Millenium Excalibur instrument following the methods described in Pitcairn et al. (2006, 2014). Analyses were carried out on the same acid digests as those used for Au analyses. Method detection limits, using acid digested blanks for 3σ, are 0.043 ppb As and 0.079 ppb Sb. Reference materials TDB-1, WMS-1 and CH-4 were used to control analytical precision and accuracy. The results are reported in Table 1.

Major and trace element analyses

Samples were analyzed for major and trace elements by ICP-MS following lithium metaborate/tetraborate fusion and total acid digestion at Activation Laboratories Ltd. (Actlabs), Canada. Analyses were carried out on a Varian Vista 735 ICP-MS and calibration was performed using 7 prepared USGS and CANMET reference materials. Loss on ignition (LOI) is determined by weight difference after ignition at 1000°C. The detection limits are between 0.001 to 0.01% for major elements, 0.005 to 5 ppm for trace elements and 0.5 ppm to 0.001% for base metals. Selected trace elements were analyzed by ICP-MS at the National Oceanography Centre Southampton (NOCS) following hydrofluoric, perchloric and nitric acid digestion. Analyses were carried out on a ThermoFisher Scientific XSeries 2 ICP-MS with accuracy and precision determined from repeated measurements of JA-2. The results are reported in Table 1.

Sr isotope analysis

Sr isotope analysis was carried out at the National Oceanography Centre Southampton (NOCS). Sample preparation procedure is the same as explained for trace elements analyses at NOCS. The mother solutions were subsampled to give approximately 1μg Sr and the Sr isolated using 50μl Sr-Spec resin columns, the column blanks were <0.1ng. The dried samples were loaded onto a single Ta filament with a Ta activator solution. $^{87}Sr/^{86}Sr$ was analyzed using multidynamic peak jumping routines on ThermoFisher Scientific Triton Plus Thermal Ionisation Mass Spectrometers with a beam size of ^{88}Sr = 2V normalized to $^{86}Sr/^{88}Sr$ = 0.1194. The long term average for NBS987 on the instrument is 0.710244±0.000019 (2sd) on 138 analyses. The results are reported in Table 2.

Stable isotope (C and O)

Carbon and oxygen isotope analyses were carried out on the carbonate fraction of serpentinite whole rock samples and 3 carbonate veins. The serpentinite samples were prepared by micro-milling of carbonate bearing areas within the serpentines to produce a carbonate rich powder. Isotope analyses were undertaken using an automated triple-collector gas source mass spectrometer (Analytical Precision AP2003) linked to an automated gas preparation device at

the Scottish Universities Environmental Research Centre (SUERC), East Kilbride. For the C isotope analyses, 2mg of the powdered whole-rocks and carbonate veins samples were reacted with 103% phosphoric acid to produce carbon dioxide, which was then purified before analysis. Samples were reacted for 96 hours at a constant temperature of 70°C. Gas mineral fractionation for dolomite was calculated following Rosenbaum and Shepherd (1986). Magnesite and mixtures of magnesite and dolomite were treated as dolomite. Precision and accuracy were monitored by reference to long-term analysis of laboratory and international standards. Precision is better than 0.2‰ at 1σ for carbon and oxygen. Results are reported as δ‰ values relative to the V-PDB and V- SMOW scales for C- and O-isotopes, respectively (Table 2).

Microthermometry

Three dolomite samples (Me2, Me12, Me28) and magnesite veinlets in serpentinite sample Me9, and one quartz sample (Me3) were selected for detailed fluid inclusion studies. The samples were prepared as 150 µm thick doubly polished sections. After careful documentation and selection of fluid inclusions, microthermometric analyses were carried out at Stockholm University using a Linkam THM 600 heating and cooling stage mounted on a Nikon microscope utilising a 40x long working-distance objective. The reproducibility was ±0.1°C for temperatures below +40°C and ±0.5°C for temperatures above 40°C. The stage was calibrated with synthetic fluid inclusion standards (SynFlinc®) and well-defined natural inclusions in Alpine quartz. The results are listed in Table 3.

Raman spectrometry

Raman spectrometry analyses were performed using a laser Raman confocal spectrometer (Horiba instrument LabRAM HR 800) equipped with a multichannel air cooled CCD detector at Stockholm University. The same set of carbonate veins prepared for microthermometry study was selected for determination of fluid composition trapped in inclusions. In addition, serpentinite samples from localities A and B were analyzed to identify serpentine minerals. An Ar-ion laser (λ = 514 nm) was used as the excitation source with an output power at the sample of 8 mW. The instrument was integrated with an Olympus microscope and the laser beam was focused to a spot of 1 µm with a 100x objective. The spectral resolution is about 0.3 cm^{-1}. The instrument was calibrated using a neon lamp and the Raman line of a silicon wafer (520.7 cm^{-1}). Instrument control and data acquisition was made with LabSpec 5 software.

[Insert Table 1 near here]

5. Results

5.1. Petrography and mineralogy

Serpentinites from locality A (referred to from this point onwards as *Lz-serpentinite*) are composed essentially of lizardite and late chrysotile veinlets with minor carbonate, opaque minerals and traces of chlorite, bastite pseudomorphs, and talc. In places, serpentine minerals retain the crystal habit of the original mafic minerals. Chrysotile occurs as long fibrous veinlets cross-cutting the lizardite matrix, indicating protracted serpentinization (Fig. 5a, b).

Carbonates are stained with iron-oxide and occur as scattered blocky aggregates or filling the mesh texture of original mafic mineral or secondary chrysotile veinlets (Fig. 5b). The opaque minerals in the serpentinites are Cr-spinel, pentlandite and magnetite. The Cr-spinels (1-3% by volume) are slightly altered and occur as deep-red grains with sub-rounded outlines. Locally the Cr-spinels show slight alteration at grain boundaries forming narrow rim of Cr-magnetite with large unaltered core (Fig. 5c). Pentlandite (1-2% by volume) is rounded and altered to garnierite and magnetite along margins. Magnetite occurs as primary scattered anhedral grains or as secondary narrow rims around Cr-spinels or defines olivine and orthopyroxene relicts.

Serpentinites from locality B (referred to from this point onwards as *Atg-serpentinite*) are composed of antigorite and carbonate with minor talc, Cr-spinel and clinochlore. Antigorite is the only serpentine mineral and occurs as flakes and shreds with no evidence of late chrysotile. In places, antigorite grains are intergrown with abundant magnesite and minor talc (Fig. 5d). The carbonates, composed dominantly as magnesite with minor dolomite occur as disseminated, cryptocrystalline veinlets, crystal clusters and infilling cracks in cases together with talc (Fig. 5d, e). Similar magnesite veins have been reported in CED serpentinites by previous workers (Ghoneim et al. 1999; Azer and Stern 2007; Ali-Bik et al. 2012). Based on SEM analysis, clinochlore is Cr-rich type (Kammererite) and occurs as aureoles around altered Cr-spinels. The opaque minerals are Cr-spinel and magnetite with no evidence of sulphide minerals such as pentlandite. The Cr-spinels (1-3% by volume) in this group of serpentinites occur as disseminated subhedral zoned grains, with small unaltered chromite core, altered ferritchromite zone and Cr-magnetite outer rim (Fig. 5f). The relict mesh texture in the Atg-serpentinites (Fig. 3b and d) suggests that these rocks originated as Lz-serpentinites.

Talc-rich rocks which in parts bear carbonate and quartz veins occur at both localities B and C comprising talc, amphibole (tremolite, anthophyllite), quartz, clinochlore, altered Cr-spinel, magnetite and traces of rutile. Talc mostly occurs as fine shreds, microcrystalline fibres and rarely as coarse- to medium-grained flakes with tremolite/anthophyllite and clinochlore (Fig. 5g, h). In the study area, highly foliated talc-schists (e.g. Me15 and Me17) are distinctive within the fault and shear zones. Syn-kinematic characteristics of these rocks include asymmetric foliation and formation of tremolite neoblast at high angle to the mylonitic textures (Fig. 5g). Chlorite occurs either as intergrowth aggregates with talc and amphibole or aureoles that enclose Cr-spinels; in the latter case, composition approaches Cr-rich clinochlore (Fig. 5h). The opaque minerals in talc-rich rocks are mostly relicts of primary Cr-spinels which have experienced brittle brecciation and pervasive alteration to ferritchromite (Fig. 5i).

[Insert figure 5 near here]

Carbonate veins in the study area vary from micro-scale networks infiltrating the matrix of the serpentinites to metre-wide veins together with quartz in talc-rich rocks (Fig. 3e).

Carbonate minerals are dominantly magnesite and dolomite with minor calcite. Both carbonates and quartz veins display evidence of shearing manifested by stretched grain ribbons, recrystallized bulges along crystal boundaries, and S-fabrics especially in fault and shear zones. Some of the carbonate (e.g. Me12) veins host minor magnetite which occurs as disseminated aggregates of fine to medium grain size and traces of accessory Cr-spinel, zircon, monazite, rutile, and apatite.

5.2. Geochemistry

Major elements variations

Lz-serpentinites contain 44.8 to 47.2 wt% SiO_2, 0.56 to 0.65 wt% Al_2O_3, 44.3 to 44.7 wt% MgO, 7.1 to 8.3 wt% total Fe as FeO and 0.8 to 1.3 wt% CaO (Table 1). The Atg-serpentinites show similar range of major elements and contain 42.2 to 46.7 wt% SiO_2, 0.15 to 0.62 wt% Al_2O_3, 44.6 to 50.5 wt% MgO, and 6.9 to 9.7 wt% total Fe as FeO (Table 1). Major element oxides in the talc-rich rocks range from 57.2 to 62.7 wt% SiO_2, 0.4 to 1.7 wt% Al_2O_3, 20.7 to 28.6 wt% MgO, 0.03 to 0.1 wt% Na_2O, 4.5 to 7.4 wt% total Fe as FeO and 2.8 to 12.9 wt% CaO, with other major oxides in minor amounts (Table 1). The protolith of the talc-rich rocks cannot be inferred from this composition. Both varieties of serpentinites contain abundant volatiles (H_2O and CO_2) with LOI values ranging from 13.2 to 14.2 wt% for Lz-serpentinites and 12.5 to 20.8 wt% for Atg-serpentinites (Table 1; Fig. 6a). Talc-rich rocks contain lower LOI values ranging from 2.1 to 4.1 wt% along with lower MgO and higher SiO_2, Na_2O and CaO than the serpentinites (Table 1; Fig. 6a, b, c).

[Insert figure 6 near here]

Compositional similarities between Lz-serpentinites and Atg-serpentinites along with relict olivines (in Lz-serpentinites) and Cr spinel indicate these formed from broadly similar harzburgite protoliths. In contrast, the major element compositions of the talc-rich rocks are unlike any mantle peridotite and only elevated MgO contents and Cr-spinel relicts suggest that this lithology may also have a harzburgite protolith.

Trace elements variations

The serpentinites analyzed in this study show relatively high concentrations of Cr, Ni and Co with mean values of 1735 ppm, 2217 ppm and 99 ppm, respectively in the Lz-serpentinites and 2293 ppm, 2308 ppm, and 103 ppm, respectively in the Atg-serpentinites (Table 1; Fig. 7). The talc-rich rocks show somewhat lower concentrations of these elements with average concentrations of 1430 ppm for Cr, 1152 ppm for Ni and 64 ppm for Co (Fig. 7).

The Lz-serpentinites show higher concentrations of incompatible trace elements Li, Rb, Ba, U, Pb, Sr) in comparison to Atg-serpentinites (Fig. 8a; Table 1). The Lz-serpentinites also

show higher S, As and Au concentrations compared with the Atg-serpentinites and talc-rich rocks (Fig. 7).

[Insert figure 7 near here]

Chondrite-normalized rare earth element (REE) patterns of different serpentinites, talc-rich rocks and carbonate veins, using the normalizing values of McDonough and Sun (1995), are presented in figure 8b, to d. The Lz-serpentinites contain higher Σ REE concentrations (~2.46 ppm) than Atg-serpentinites (~0.08 ppm). The carbonate veins show the highest Σ REE concentrations (~63 ppm), and the talc-rich rocks show intermediate concentrations (~ 1.1 ppm) between the two varieties of serpentinites (Table 1; Fig. 8b-d). The Lz-serpentinites are characterized by moderate enrichment of LREE/HREE (La_N/Yb_N ~11) and Atg-serpentinites show slight depletion in MREE with a strong positive Eu anomaly. Sample Me24 is distinct from the other Lz-serpentinites considering lower REE enrichment and MREE depletion similar to Atg-serpentinites. The carbonate veins generally show flat REE patterns with slight LREE enrichment (La_N/Yb_N = 11.3) in sample Me2. The talc-rich rocks REE patterns are approximately flat with slight enrichment in LREE (La_N/Yb_N = 3.55 in average) and a slight positive Eu anomalies (Fig. 8c). A comparison between average compositions of different rock types and veins is show in figure 8d.

[Insert figure 8 near here]

5.3. Isotopic signature of Meatiq carbonate altered rocks and veins

Results for carbon and oxygen isotope analysis for carbonate fraction of nine serpentinites samples, Rb and Sr concentrations and $^{87}Sr/^{86}Sr$ ratios for nine whole-rock serpentinite samples, and three carbonate veins are listed in Table 2 and plotted in figure (9a-c). $^{87}Sr/^{86}Sr$ ratios have been corrected for 600 Ma of radiogenic growth, which represents the best estimate for the timing of carbonation occurred in the CED (Stern and Gwinn 1990).

[Insert Table 2 near here]

The initial $^{87}Sr/^{86}Sr$ ratios vary from 0.7028 to 0.7078 (Table 2). The low $^{87}Rb/^{86}Sr$ in all samples indicates that uncertainties in the age correction are unlikely to introduce significant errors, but low Sr contents of especially Atg-serpentinites makes these especially vulnerable to minor alteration by groundwater or biological activity. Initial $^{87}Sr/^{86}Sr$ for samples containing <10 ppm Sr should therefore be regarded with suspicion. Three of the four samples that contain <10 ppm Sr show the highest initial $^{87}Sr/^{86}Sr$ (0.7067 – 0.7078); these contrast with much lower initial $^{87}Sr/^{86}Sr$ for three Lz-serpentinites and carbonate veins (0.7028 – 0.7046) and we interpret these high concentrations as the product of secondary processes. The $\delta^{18}O$ values range from +6.4‰ to +15.1‰ while $\delta^{13}C$ values vary between -8.1‰ to -4.1‰ (Table 2). The carbonate veins show tightly clustering isotopic values with

$\delta^{13}C$, $\delta^{18}O$ and initial $^{87}Sr/^{86}Sr$ values ranging from -8.1‰ to -6.8‰, +6.4‰ to +10.5‰, and 0.7028 to 0.7034 respectively (Table 2). They contain low concentrations of Rb from 0.001 to 0.04 ppm (mean = 0.015 ppm) while their Sr contents are high and variable, from 503 to 2365 ppm (mean = 1334 ppm). The $^{87}Rb/^{86}Sr$ ratios are extremely low, invariably less than 0.0001.

[Insert figure 9 near here]

The carbonate fraction of serpentinites have higher C and O isotopic values compared to carbonate veins. The serpentinites also show higher $^{87}Sr/^{86}Sr$ ratios compared to the carbonate veins (Table 2; Fig. 9a-c). The carbonate fraction of Lz-serpentinites (Me21 to Me24) range in $\delta^{18}O$ from +12.3‰ to +15.1‰ with uniform $\delta^{13}C$ values range between -4.2‰ to -4.1‰. Their whole rock $^{87}Sr/^{86}Sr$ ratios span a modest range from 0.70421 to 0.70622. They contain low concentrations of Rb from 0.033 to 0.12 ppm (mean = 0.88 ppm) and Sr concentrations ranging from 5.8 to 70 ppm (mean = 37.6 ppm) with Rb/Sr ratios mostly less than 0.05. The carbonate fraction of Atg-serpentinites (Me5 to Me9) show $\delta^{18}O$ values that range from +10.3‰ to +11.5‰ and $\delta^{13}C$ values ranging from -5.3‰ to -5.9‰ (Table 2). Their whole rock $^{87}Sr/^{86}Sr$ ratios vary from 0.70396 to 0.70585 (Table 2). The Atg-serpentinites contain lower concentrations of Rb (mean = 0.023 ppm) and Sr (mean = 0.36 ppm) in comparison to Lz-serpentinites. Their Rb concentrations range from 0.009 to 0.031 ppm and their Sr concentrations vary from 0.23 to 0.45 ppm with Rb/Sr ratios vary from 0.22 to 0.35 (Table 2).

5.4. Microthermometry

Five samples of carbonate and quartz veins were collected for fluid inclusion microthermometry. Sample Me2, Me12 and Me28 are dolomite veins, sample Me9 is from a magnesite vein in Atg-serpentinite sample and Me3 is from a quartz vein. Microthermometric data are given in Table 3.

Fluid inclusion types

Three fluid inclusion types (I to III) have been identified (Table 3; Fig. 10a-c). Some fluid inclusions occur along secondary trails (Fig. 10d) and necking down is occasionally seen (Fig. 10e). In cases, inclusions show shear sense due to local tectonic activity (Fig. 10f). All analyses were made on fluid inclusions without clear signs of post-entrapment modifications.

Type-I inclusions are aqueous two-phase inclusions (LH_2O+ VH_2O) occurring as primary and secondary inclusions with variable degrees of fill (~5-60 vol% gas). They are elongated with rectangular to negative crystal shapes with a size from 4 to 40 µm (Fig. 9a). Some inclusions are single phase (VH_2O). Type-II inclusions are primary three-phase (LH_2O+LCO_2+VCO_2) aqueous-carbonic with low degree of fill (~30 to 70 vol% gas). They are negative crystal or irregular shaped and range in size from 5 to 15 µm (Fig. 10b). Type-III inclusions are

carbonic (LCO_2 + VCO_2), less than 10 μm in size, rounded to negative crystal in shape and occur in cluster or along trails (Fig. 10c). Type-III inclusions are only present in a quartz vein (Me3).

Fluid inclusions hosted by carbonate veins

Type I inclusions: In Me2 final ice-melting temperatures (Tmice) range from -2.6°C to 0.0°C which gives a salinity of 0.0 to 4.3 mass% NaCl eq. (low salinity inclusions) and from -16.4°C to -4.0°C which corresponds to 6.4 to 16.9 mass% NaCl eq. (moderate salinity inclusions). Salinities are calculated using data in Bodnar (2003). The temperatures of first ice-melting (Tfmice), around -35°C for the low salinity assemblage, and about -50°C for the moderate salinity inclusions are similar to eutectic temperatures of H_2O-salt systems dominated by NaCl-$MgCl_2$ and $CaCl_2$-NaCl respectively (Shepherd et al. 1985). Homogenization temperature of all inclusions to liquid occurred between 161°C and 383°C. In Me9, first melting of the type-I inclusions was observed around -35°C which suggests a salt composition dominated by NaCl and $MgCl_2$ (Shepherd et al. 1985). Final ice-melting temperatures range from -2.4°C to -0.5°C corresponding to a salinity of 0.9 to 5.5 mass% NaCl eq. Total homogenization to liquid occurred at temperature between 210°C and 335°C.

[Insert Table 3 near here]

Type II inclusions: In Me12, there was no separate CO_2 phase, but CO_2 clathrate melting (Tmclath) occurred in the range from 7.5°C to 9.8°C which indicates a salinity of 0.2 to 4.9 mass% NaCl (Fall et al. 2011). Total homogenization to liquid occurred in the temperature range 252°C to 276°C. In Me28, melting of the frozen CO_2 ($TmCO_2$) occurred between -57.3°C and -56.6°C and homogenization of the CO_2-phase to liquid took place between +26.8°C and +29.2°C. CO_2 clathrate melting was observed at temperatures between +6.6°C and +10.0°C which indicates a salinity of 0.0 to 6.8 mass% NaCl. Total homogenization to liquid phase occurred between 242°C to 331°C.

[Insert figure 10 near here]

Fluid inclusions hosted by quartz veins

Type I inclusions: In Me3, first observed melting around -35°C suggests a predominant NaCl-$MgCl_2$ composition. Final ice-melting from -3.5°C to -0.1°C corresponds to a salinity of 0.2 to 5.7 mass% NaCl eq. Total homogenization occurred at temperatures ranging from 225°C to 266°C (to liquid) except for the secondary inclusions which homogenized between 177°C to 234°C (to liquid).

Type-II and III inclusions yield melting temperatures for CO_2 from -57.7°C to -56.6°C and homogenization of CO_2 to liquid, between +26.8°C to +29.5°C. The temperatures indicate the presence CH_4 and/or N_2 in addition to CO_2. Based on the data in van den Kerkhof and Thiéry (2001), the corresponding molar volumes of the CO_2 inclusions range from about 65 to 90 cm^3/mole. Melting of CO_2 clathrate occurred at temperatures between +7.7°C to +9.5°C

which indicates a salinity of 1.0 to 4.7 mass% NaCl eq. Total homogenization to liquid phase occurred between 305°C to 365°C.

6. Discussion

In the following, we explore the significance of our results in relation to: 1) provenance of the ophiolites; 2) condition of serpentinization; 3) talc-rich rocks formation; 4) the composition of the carbonating fluid and the conditions of alteration; 5) the sources of the CO_2-rich carbonating fluid; 6) element mobility during serpentinization and listvenitization; and 7) the evolution of serpentinization and carbonation and the implications for formation of Au deposits.

6.1. Provenance of the ophiolites

Ophiolites and ophiolitic rocks are remarkably abundant in the Arabian-Nubian Shield (Fig. 1). Three main tectonic settings have been proposed for formation of the ophiolites in the ANS; (i) mid-ocean ridges (Zimmer et al. 1995; Khalil and Azer 2007); (ii) back-arc basins (Bakor et al. 1976; Kröner 1985; Pallister et al. 1988; El-Sayed et al. 1999; Farahat et al. 2004; El Gaby 2005; El Bahariya 2008; Abd El-Rahman et al. 2009; Ali et al. 2009), and (iii) forearcs (Stern et al. 2004; Azer and Stern 2007; Hamdy et al. 2013; Ahmed 2013; Khedr and Arai 2013; Azer 2014; Khalil et al. 2014; Abu-Alam and Hamdy 2014). Serpentinized peridotites investigated in this study are depleted in Al_2O_3 and CaO and plot within the field of metamorphic peridotites associated with ophiolitic suits (Fig. 11a; Coleman 1977), similar to harzburgites from modern intra-oceanic forearcs (Fig. 11b).

[Insert figure 11 near here]

In completely serpentinized peridotites without relicts of primary silicate minerals, a good proxy to determine original tectonic setting is the composition of Cr-spinel cores (Irvine 1965; Arai 1992; Dick and Bullen 1984). Cr-spinels resist alteration and are widely used to constrain tectonic settings where ophiolites formed. According to Dick and Bullen (1984), peridotites that contain Cr-spinel with Cr# >0.6 are commonly restricted to subduction-related rocks. The Cr# of the Cr-spinel cores in the investigated Lz-serpentinites is mostly >0.6 and lie in the compositional space for Cr-spinels of forearc peridotite (Supplementary Table; Fig. 11.c). This is similar to recent studies on Cr-spinels from the Fawakhir serpentinites in the vicinity of study area (~7 km north of study area A) and other serpentinites in the ED that are considered to have formed in the forearc of a supra-subduction zone (SSZ) setting (Azer and Stern 2007; Hamdy et al. 2013; Azer 2014; Abu-Alam and Hamdy 2014).

6.2. Conditions of serpentinization

Lizardite, antigorite and talc have been widely reported in ED serpentinite bodies (Basta and Kader 1969; Akaad and Noweir 1972; Abu-Alam and Hamdy 2014), but the relationships between these minerals and their significance in terms of the conditions of alteration remain

unclear. As noted in the results section, serpentinites investigated in this study can be classified into 2 distinct groups; Lz-serpentinites, and Atg-serpentinites. In Lz-serpentinites, lizardite and chrysotile assemblages become major rock forming minerals with minor carbonate and relatively fresh Cr-spinel. Lizardite and chrysotile form at lower temperature alteration conditions than antigorite (Mellini et al. 1987; Scambelluri et al. 1995; O'Hanley 1996; Trommsdorff et al. 1998; Andréani et al. 2007; Evans 2004, 2010). The recent study of Schwartz et al. (2013) shows that at below 300°C, lizardite and locally chrysotile are the dominant serpentine species commonly forming a mesh texture, and that between 320°C and 390°C, lizardite is progressively replaced by antigorite which is the sole stable serpentine mineral at temperatures >390°C. The extent of spinel alteration suggests similar alteration conditions, with thin outer magnetite rims in sharp contact with Cr-spinel core suggesting sub- to lower-greenschist facies condition (Farahat 2008). This alteration zoning of Cr-spinel together with abundant lizardite and chrysotile assemblages forming a mesh texture and lack of higher temperature serpentine phase (i.e. antigorite) indicates sub-greenschist facies conditions and temperatures <300°C (Abzalov 1998; Barnes 2000; Farahat 2008).

In the Atg-serpentinites, antigorite and carbonate assemblages become major rock forming minerals with minor talc, altered Cr-spinel, and clinochlore. The antigorite is the sole serpentine mineral in these rocks and the lack of lizardite and chrysotile indicates the transition of these phases to antigorite. Cr-spinels are concentrically zoned with small, unaltered cores, well-developed transitional zone of ferritchromit and thick Cr-rich magnetite rims (Fig. 5f). The occurrence of antigorite as the sole serpentine phase together with alteration textures of Cr-spinel indicate upper greenschist conditions and temperatures >450°C (Abzalov 1998; Barnes 2000).

A number of different mechanisms have been suggested for the transition of lizardite to antigorite. In a water-saturated open system, the transition of lizardite to antigorite can be written as (following Vils et al. 2011):

lizardite + SiO_2(aq) → antigorite + H_2O reaction 1

(Coleman 1971; Evans 2004) or alternatively in closed system with no inlet fluid, the transition of lizardite to antigorite can be written as:

lizardite → antigorite + MgO(aq) + H_2O reaction 2

The extensive carbonate alteration and intimate intergrowth between antigorite and magnesite indicate that the generation of antigorite was most likely related to precipitation of carbonate from a CO_2-bearing fluid. Therefore, the lizardite to antigorite transition must have occurred in the presence of CO_2. Reaction 2 would facilitate generation of magnesite due to liberation of aqueous MgO. The Atg-serpentinites contain higher MgO and LOI and slightly lower SiO_2 compared to Lz-serpentinites (Fig. 6), which is consistent with the addition of MgO and CO_2 to these rocks. We suggest that the lizardite to antigorite transition was contemporaneous

with magnesite crystallization due to influx of CO_2-rich fluid at temperatures above the stability field of lizardite (i.e. >300˚C; Evans 2004; Schwartz et al. 2013).

6.3. Conditions of Listvenitization

Listvenite is formed by low to intermediate temperature hydrothermal/metasomatic alteration of mafic-ultramafic rocks (especially serpentinites), commonly associated with major fault and shear zones (Uçurum 2000; Akbulut et al. 2006). The listvenitic rocks investigated in this study occur in localities B and C and are spatially associated with shear zones. These rocks show gradational to sharp contacts with the surrounding serpentinite (Figs. 3d, 4) indicating that the listvenites formed after serpentinization. This relationship is commonly described elsewhere (Böhlke 1989; Griffis 1972; Uçurum 2000; Hansen et al. 2005, Boschi et al. 2006) and in the ED (Ghoneim et al. 2003; Azer 2013; Zoheir and Lehmann 2011; Emam and Zoheir 2013) and is supported by several experimental studies on a MgO-SiO_2-H_2O-CO_2 system (Johannes 1969; Klein and Garrido 2011; Klein and McCollom 2013; Bjerga et al. 2015). In the study area, listvenitic rocks show variable mineral assemblages including talc-tremolite assemblages with minor ferritchromite and clinochlore in the highly foliated talc-rich rocks (Fig. 3e, 5g), and talc-tremolite-anthophyllite assemblages together with ferritchromite and clinochlore where foliation is less well-developed (Fig. 5h). The listvenitic zones also contain quartz and carbonate (with minor talc) veins (Fig. 3e).

In ultramafic rocks, the talc-tremolite (± magnesite) assemblages are indicative of upper-greenschist to low-amphibolite facies (Johannes 1969; Barns 2000; Will et al. 1990). But at mid-amphibolite facies and relatively low pressure (<2kbar), the stability limit of former assemblages is exceeded and stable assemblages are talc-tremolite-anthophyllite (Will et al. 1990; Evans and Guggenheim 1988). Anthophyllite is a common phase in the middle and upper amphibolite facies of ultramafic rocks (Will et al. 1990; Barns 2000). However, the occurrence of stable talc-tremolite-anthophyllite assemblages could also be related to higher SiO_2-H_2O activity in the fluid (Evans and Guggenheim 1988). So, the carbonate-poor nature of the talc-tremolite-anthophyllite assemblages in our shear zone samples may presumably be related to either higher temperature or higher activity of SiO_2 and H_2O in the altering fluid, or a combination of both phenomena in some parts of the shear zones.

The talc-rich rocks most likely form from breakdown of Atg-serpentinites that host these rocks. This is supported by mineralogy and mineral textures in Atg-serpentinites where cross-cutting micro-veins of magnesite and talc occur in some samples (Fig. 5e). Such a conversion has been shown to occur in the presence of CO_2-rich fluid (more than 2-6 mol% CO_2 and under fluid pressure of 2 kbar, Johannes 1969) at temperatures above 300°C (e.g. Schandl and Naldrett 1992; Hansen et al. 2005; Robinson et al. 2005):

$$2Mg_{48}Si_{34}O_{85}(OH)_{62} + 45CO_2 \rightarrow 45MgCO_3 + 17Mg_3Si_4O_{10}(OH)_2 + 45H_2O \qquad \text{reaction 3}$$

(antigorite) (magnesite) (talc)

Much of the magnesite formed by this reaction appears to occur in discrete veins and pods within the listvenitic rocks or as veinlets crosscutting Atg-serpentinites (Fig. 3e, 5e). This

reaction is supported by the chemical compositions of the rocks as the talc-rich rocks are strongly depleted in volatiles and MgO relative to the serpentinites (Fig. 6). Talc-rich rocks contain an average of ~2.9 wt% LOI compared to average of ~15.2 wt% LOI in the serpentinites indicating that, as is suggested by reaction 3, the listvenitization process involves dehydration. Reaction 3 shows that MgO is balanced during the listvenitization process but that much of the MgO occurs in the discrete veins of magnesite with the surrounding talc-rich rocks being relatively depleted in MgO. Enrichments in SiO_2 and CaO in the talc-rich rocks are in the proportions expected through residual concentration due to the loss of volatiles and MgO (Fig. 6).

6.4. *The composition of the carbonating fluid and the conditions of alteration*

The conditions at which the carbonate alteration occurs can be estimated through fluid inclusion microthermometry vein carbonate. The carbonate veins were formed from aqueous and carbonic fluids with a large range in relative proportions from pure aqueous to pure carbonic end-members indicating coexisting, immiscible fluid phases at the time of carbonate deposition. The carbonic phase has a CO_2-rich composition with small amounts (0 to 5 mole%) of dissolved CH_4, probably present as a result of serpentine mineral alteration reactions, and N_2 of unknown origin. The aqueous phase in both carbonate and quartz veins has low salinity (<7 eq. mass% Mg-Na-Cl; Table 3). Some aqueous inclusions in sample Me2 have higher salinities (up to 17 eq. mass% NaCl) and a more Ca-Na-Cl dominated composition. These may represent local input of a more saline fluid from external source.

[Insert figure 12 near here]

Total homogenization temperatures of the samples range from 161°C to 383°C (Table 3). Primary inclusions have a more limited range of total homogenization temperatures from 225°C to 383°C (Table 3), with secondary aqueous fluid inclusions in healed microfractures showing lower homogenization temperatures (161°C to 255°C; Table 3). Total homogenization temperature for primary fluid inclusions trapped under conditions of immiscibility is interpreted to represent the original formation temperature (Diamond 2003; Bodnar 2003). The trapping temperature and pressure conditions can be estimated from compositions of the two end-members (Diamond 2003). Trapping conditions for immiscible fluids can be determined by using the technique of intersecting isochores (Roedder 1984) and at the intersecting point in the PT-diagram which two end-members have temperature and pressure that are identical. The isochore to be used for the aqueous end-members (inclusions with the lowest homogenization temperature) in the samples is based on the data in Bodnar (2003) for aqueous fluid inclusions with homogenization temperature of about 225°C and a salinity of 0-7 eq. mass% NaCl. The isochores for the carbonic end-member (after data in Van den Kerkhof and Thiéry 2001) are for molar volumes of 65 and 90 cm^3/mole (Fig. 12). The intersection of the aqueous and carbonic isochores in the PT diagram gives trapping conditions for carbonate veins of the study area within a temperature interval from 270°C to

300°C and at a pressure of 0.7 to 1.1 kbar. The pressure corresponds to lithostatic depths of 2.6 to 4.2 km (Fig. 12).

6.5. The sources of the CO_2-rich carbonating fluid

The carbonate vein samples have $\delta^{13}C$ (mean = -7.2‰) and $^{87}Sr/^{86}Sr$ (mean = 0.7030) compositions that fall within the range of mantle-derived carbon (Taylor et al. 1967; Deines 1989; Demény et al. 1998; Fig. 9a). The $\delta^{18}O$ values of these veins (ranging from +6.4 to 10.5‰) are slightly heavier than depleted-mantle values (i.e. +5.5±0.2‰; Elier 2001) indicating partial re-equilibration with crustal brines, groundwater or seawater (Fig. 9b). The robust $^{87}Sr/^{86}Sr$ compositions in the carbonate veins are indistinguishable from initial ratios for Neoproterozoic mantle-derived igneous rocks of the Arabian-Nubian Shield (Engel et al. 1980; Fitches et al. 1983; Stern and Hedge 1985; Stern and Gwinn 1990; Fig. 13.) Based on $\delta^{13}C$ and $^{87}Sr/^{86}Sr$ values, the carbonate veins most likely formed from mantle-derived CO_2-bearing fluids. An alternative explanation is that the veins formed from surface-derived fluids that fully equilibrated with the host rock. However in that case, one would expect full equilibration of O and perhaps Sr isotopes (e.g. Falk and Kelemen 2015), but that C isotopes would preserve the fluid signature. The data show the opposite with more crustal signatures shown in the O isotopes than in C isotopic compositions. Furthermore the fluid inclusion data shows that the carbonation was produced by a mixture of H_2O and CO_2 fluids with the primary inclusions including pure CO_2 end member fluids at around 270°C to 300°C. It is difficult to conceive how such a fluid could originate as meteoric water or seawater.

[Insert figure 13 near here]

The carbonate fraction in the Lz- and Atg-serpentinites have $\delta^{13}C$ compositions (-5.9 to -4.1‰) that also falls within the range of depleted mantle carbonate (i.e. Taylor et al. 1967; Deines 1989; Fig. 9a), and are close to the isotope ratios of mantle C ($\delta^{13}C$ ~-5‰) (Deines 2002). The $\delta^{18}O$ compositions of carbonate fraction in Lz- and Atg-serpentinites and $^{87}Sr/^{86}Sr$ ratios in whole rock Lz- and Atg-serpentinites plot outside depleted mantle values. These sample values plot on mixing lines between mantle fluid and sedimentary carbonate indicating incorporation of surface-derived O and Sr (Fig. 9c). The carbonate fraction in Lz-serpentinites shows consistently higher $\delta^{18}O$ (the highest $\delta^{18}O$ values in this study, ranging from 12.1 to 15.1‰) and more radiogenic Sr for whole rock values compared to carbonate veins, suggesting interaction with a greater proportion of surface derived fluid (Fig. 9b). A possible interpretation is that the heavier $\delta^{13}C$ values (-4.2‰) of carbonate fraction in Lz-serpentinites compared to Atg-serpentinites ($\delta^{13}C$ = -5.5‰) might reflect interactions with fluid having low C/O ratio causing a shift in $\delta^{18}O$ with little change in $\delta^{13}C$ (-1.3‰ higher). Both varieties of serpentinite contain carbonate fractions that most likely represent mixtures of mantle derived, and surface derived CO_2.

6.6. *Element mobility during serpentinization and listvenitization*

As discussed above, the major element changes during the different styles of alteration in these rocks are dominated by addition and removal of CO_2 and H_2O, and in the remobilization of SiO_2 and MgO. Variations in the other major elements are most easily explained by residual enrichments caused by addition of carbonate to the rock. The extent of recrystallization during the alteration of serpentinite and talc-rich rock also redistributed trace elements with some being locally remobilized in the rock and other elements flushed out the rock. The Cr-spinels for example are recrystallized during alteration, but Cr was only locally redistributed into nearby neoblasts of Cr-bearing magnetite and clinchlore (Fig. 5c, f, i). Primary Ni-sulphides such as pentlandite found in the Lz-serpentinites are absent from the Atg-serpentinites and the talc-rich rocks. The pentlandite broke down to Ni-bearing magnetite (Fig. 14a, b), most likely during the transition from lizardite to antigorite. The Ni released was locally redistributed in the rock (Fig. 7), but the S and perhaps other trace elements were flushed from the rock. The removal of S from the rock is shown through the large decrease in S content between the Lz-serpentinites (~447 ppm) and Atg-serpentinites (~16 ppm; Fig. 7).

[Insert figure 14 near here]

The REE show interesting variability in the serpentinites, talc-rich rocks and carbonate veins. Carbonate veins are the most enriched in REE and in fact show higher concentrations of incompatible trace elements (Pb, Sr, Ba, HFSE, Th and Y) than the serpentinites (Fig. 8a to d) Thin-section and SEM studies reveal that these veins contain disseminated zircon, apatite, monazite and rutile that hold these elements (Fig. 14c, d). The texture and paragenetic sequence of monazite and rutile (Fig. 14d) indicate they precipitated from the carbonate fluid. Several studies have shown that CO_2-rich fluids promote REE mobilization mainly as REE-carbonate complexes (Tsikouras et al. 2006; Tsay et al. 2014; Chen and Zho 2015). The Atg-serpentinites and talc-rich rocks show lower REE concentrations than the Lz-serpentinites (Fig. 8d). We suggest that REEs were remobilized by the CO_2-bearing fluids accompanying formation of antigorite from lizardite and during listvenitization, as has been suggested previously (e.g. Vils et al. 2011; Kodolányi and Pettke 2011; Debret et al. 2013). The higher concentration of REE in talc-rich rocks relative to Atg-serpentinites (Fig. 8d) may also be attributed to REE uptake in the secondary mineral phases such as tremolite and anthophyllite. It has been shown that amphiboles can incorporate significant amounts of REE at hydrothermal temperatures (e.g. Gillis and Meyer 2001; Boschi et al. 2006).

There has been considerable recent research into the enrichments of fluid-mobile elements (FME) in serpentinites formed in mantle wedge settings above subduction zones (e.g. Hattori and Guillot 2003, 2007; Deschamps et al. 2011, 2012). These studies show that the FME which include B, Li, S, As, Rb, Sr, Sb, Cs, Ba, Pb, and U are enriched in mantle wedge serpentinites due to release from metamorphic dehydration reactions in the subducting slab (Deschamps et al. 2013 and references therein), and that mantle wedge serpentinite can act as a temporary residence for the FME until breakdown of antigorite occurs at temperatures

>600°C (Deschamps et al. 2013 and references therein). The FME are suggested be retained in the serpentinite minerals with only minor release during the lizardite to antigorite transition (Deschamps et al. 2013), but our results do not support this conclusion. A comparison of FME and Au concentrations between Lz- and Atg-serpentinites investigated in this study is shown in figure 15. Both varieties of serpentinites are characterized by significant enrichment in some FME such as As, Sb and Cs compared to primitive mantle (McDonough and Sun 1995) and depleted mantle values (Salters and Stracke 2004). With the exception of Sb and Cs, all of the FME shown in figure 15 have lower concentrations in the Atg-serpentinites compared to the Lz-serpentinite suggesting that these elements were mobilized during the lizardite-antigorite transition.

Gold concentrations show similar variations to some FME (Fig. 15). Gold concentrations in both varieties of serpentinite range from 0.8 to 12.6 ppb and are commonly higher than Au contents in serpentinized mantle peridotite (i.e. ~3-5 ppb; Buisson and Leblanc 1987), average of ophiolitic rocks (i.e. ~2.8 ppb; Foster 1991), and the depleted mantle (i.e. ~1 ppb; Salters and Stracke 2004). Similar to the case for S, Lz-serpentinites contain more Au (~8.0 ppb) compared to Atg-serpentinites (~2.3 ppb, Fig. 7 and 15). The similar behavior of Au and S suggests that both may reside in nickel-sulphides in harzburgites and Lz-serpentinites, as has been suggested by previous research into ANS ophiolitic serpentinites (Takla and Surour 1996; Khalil et al. 2003; Emam and Zoheir 2013). A recent study by Ferraris and Lorand (2015) in the Lherz peridotites suggests olivine as one of the main potential host minerals for gold in the ultramafic rocks. This study showed that up to 80% of the gold in these samples occurs in form of nano-inclusions within olivine, whereas only 20% of the whole-rock Au-budget occurs within Cu–Fe–Ni sulphides (Ferraris and Lorand 2015). The Au in Lz-serpentinites most likely sits within altered olivine grains or within Ni-sulphides with the decrease of whole rock Au concentrations during lizardite-antigorite transition indicating liberation of this Au by the CO_2-rich fluid. This is the first time that Au has been observed to be remobilized during lizardite-antigorite transition.

[Insert figure 15 near here]

Listvenitic rocks have long been considered an indicator of Au mineralization, but the relationship between Au and listvenite is unclear. Compared to Atg-serpentinite, the talc-rich rocks in our study show lower concentrations of Au (~0.7 ppb), As (all values below detection limit except for Me1) and S, suggesting that intense alteration of the serpentinites to form talc-rich rocks within shear zones was accompanied by fluid migration that depleted these rocks in Au, As and S. In other studies, listvenites are suggested to host Au mineralization (e.g. Halls and Zhao 1995). A number of Au deposits in the ANS such as the Barramiya deposit (Fig. 2) occur in part within shear-hosted listvenite (Zoheir and Lehmann 2011). At these localities, the listvenites are enriched in sulphides and Au (e.g. Azer 2013). Our study suggests that Au is removed from Lz-serpentinites when these convert to Atg-serpentinites, which may happen synchronous with carbonation and shearing events. As

listvenitic rocks are concentrated in fault and shear zones, element mobility is prone to overprinting continuous fluxes of fluids through these channels. We suggest that the association between Au mineralization and listvenitization may be due to their soft permeable nature which provides strong rheological contrast with more coherent rocks such as granitoids that commonly occur in contact with listvenites in ANS Au deposits (e.g. Zoheir and Lehmann 2011; Azer 2013; Zoheir and Moritz 2014).

6.7. The evolution of serpentinization and carbonation and the implications for formation of Au deposits

The samples investigated in this study show a systematic evolution in the conditions and intensity of fluid-driven alteration of the ultramafic portions of the ophiolitic fragments near the Meatiq area. The Lz-serpentinite samples represent the "least altered" serpentinites. The stability of lizardite in these rocks indicates that alteration occurred at temperatures lower than 300°C. The stable and radiogenic isotope compositions in Lz-serpentinite samples suggest that their alteration was driven by influx of a mixed mantle- and surface-derived hydrous fluid. In contrast, Atg-serpentinites contain abundant intergrown antigorite and carbonates, which combined with the textures of Cr-spinel indicates higher temperature alteration. The relict mesh texture in the Atg-serpentinites (Fig. 3b and d) indicates that these rocks originated as Lz-serpentinites. The transition of lizardite to antigorite was most likely driven by influx of CO_2-bearing fluids (Fig. 16). Shear zones within the Atg-serpentinite host listvenitic rocks including the quartz-carbonate veins. The talc-rich rocks most likely formed from breakdown of antigorite in the presence of CO_2 and during shear deformation possibly related to Najd deformation ~600 Ma. Fluid inclusions from shear zone carbonate and quartz vein samples indicate precipitation at 270°C to 300°C and 0.7 to 1.1 kbar which corresponds to lithostatic depths of 2.6 to 4.2 km for talc-rich rocks. Carbonate veins preserve the clearest signature of the fluid source with C and Sr isotopes indicating a mantle-derived CO_2 source. Figure 16 summarizes the evolution of serpentinization and listvenitization due to mantle-driven CO_2 fluid and associated element mobility in forearc settings.

[Insert figure 16 near here]

The chemical effects of the alteration process are dominated by addition of volatiles and removal of some trace elements including FME, S and Au that were strongly mobilized during the alteration process. These elements are enriched during initial serpentinization but are removed during flushing by a mantle-derived CO_2-bearing fluid travelling through shear zones accompanying formation of antigorite. The extent of carbonate alteration in ANS ophiolitic fragments indicates that mass of metals mobilized during the lizardite-antigorite transition must have been significant. Atg-serpentinites thus may be the source for some ANS Au deposits. Continued flow of the metal-bearing CO_2-rich fluid along shear zones promoted listvenitization and further leaching of metals from the serpentinites. The deposition of Au from this fluid could have occurred in locations where fluid compositions changed abruptly or in regions of rheological contrast where porosity is developed, in upflow zones, or in the

vicinity of chemically reactive rocks such as carbonaceous shales (Harraz 2000; Botros 2004; Zoheir and Lehmann 2011; Azer 2013; Zoheir and Moritz 2014).

There are few stable isotope compositions of vein minerals in ANS Au deposits but what is available shows similarities to results obtained in this study. Vein carbonate from the diorite-hosted Romite deposit in the Southern Eastern Desert (Fig. 2) has $\delta^{18}O$ ranging from 7 to 9 ‰ and $\delta^{13}C$ from -4.6 to -3.1 ‰ (Zoheir 2012). The El Sid deposit occurs on the margins of a granitoid intrusion into a carbonaceous shale; a listvenite-bearing shear zone yields O and C isotope compositions of vein carbonate of between 4.9 to 7.4 ‰ $\delta^{18}O$ and -14.7 to -13.9 ‰ $\delta^{13}C$, respectively (Zoheir and Moritz 2014). These values are similar to those in the carbonate altered ophiolitic rocks investigated in this study except for the very low $\delta^{13}C$ values at El Sid which are interpreted to be due to interaction between ore fluids and the carbonaceous shale (Zoheir and Moritz 2014). Fluid inclusion compositions from these mineral deposits yield similar aqueous carbonic fluids with similar homogenization temperatures to our results.

7. Conclusions

We investigated the causes and effects of carbonate alteration of Neoproterozoic ultramafic rocks in the Central Eastern Desert of Egypt. The samples studied from three areas around the Meatiq Dome show evolution in the extent and conditions of alteration from least altered lizardite serpentinites with mesh-textured alteration and late stage chrysotile veins to antigorite serpentinite with abundant antigorite intergrown with magnesite, dolomite and minor talc to talc-tremolite and talc-tremolite-anthophyllite assemblages in foliated talc-schists and talc-rich rocks. The listvenitic rocks occur in shear zones and contain carbonate and quartz veins. The sequence from lizardite serpentinite to antigorite serpentinite and different listvenitic assemblages represents evolving conditions of alteration from below 300°C to above 400°C, and an increase in shear stress with variable activity of CO_2, SiO_2 and H_2O in the fluid. We suggest that this evolution was synchronous with and partly controlled by influx of an aqueous carbonic fluid. The fluid composition is inferred from fluid inclusion compositions in carbonate and quartz veins in the talc-rich bodies show carbonic (CO_2±CH_4±N_2) and aqueous-carbonic (H_2O-NaCl-CO_2±CH_4±N_2) fluid inclusions with low salinity, with trapping conditions of 270°C to 300°C and 0.7 to 1.1 kbar. Stable (C, O) and radiogenic (Sr) isotope compositions suggest that the carbonating fluid was a mantle-derived CO_2-rich fluid that mixed with surficial fluid. The extent of carbonate alteration suggests that fluxing of mantle CO_2 was significant, although we cannot yet constrain how long the carbonation event lasted. Carbonation was associated with shearing and probably related to Najd deformation at ~600 Ma.

The Lz-serpentinites are enriched in Au, As, S and other fluid-mobile elements relative to primitive and depleted mantle. The extensively carbonated Atg-serpentinites contain less of these elements than the Lz-serpentinites suggesting that they were removed during carbonate alteration. The listvenitic bodies are even more depleted. We suggest that these elements were removed from the altered serpentinites by the infiltrating CO_2-bearing fluid. Fluid inclusion and stable isotope compositions of Au deposits in the CED are similar to those from

the carbonate veins investigated in this study and we suggest that carbonation of ultramafic rocks in the ophiolitic fragments in the ANS due to influx of mantle-derived CO_2 fluid produced Au-bearing fluids that contributed importantly to the formation of the Au-deposits in the ANS.

Acknowledgements

IKP acknowledges funding by the Swedish Research Council (Vetenskapsrådet Personal Research Grant PRG 621-2007-4539), SIDA (Swedish Research Links Grant 2014-4290) and the Bolin Centre for Climate Research.

References

- Abd El-Rahman, Y., Polat, A., Dilek, Y., Fryer, B.J., El-Shrkawy, M., and Sakran, S., 2009, Geochemistry and tectonic evolution of the Neoproterozoic incipient arc-forearc crust in the Fawakhir area, central Eastern Desert of Egypt: Precambrian Research, v. 175, p. 116-134.
- Abd El-Rahman, Y., Polat, A., Dilek, Y., Kusky, M.T., El-Sharkawi, M., and Said, A., 2012, Cryogenian ophiolite tectonics and metallogeny of the Central Eastern Desert of Egypt: International Geology Review, iFirst, p. 1-15.
- Abd El-Rahman, Y., Polat, A., Fryer, B.J., Dilek, Y., El-Sharkawy, M., and Sakran, S., 2010, The provenance and tectonic setting of the Neoproterozoic Um Hassa Greywacke Member, Wadi Hammamat area, Egypt: Evidence from petrography and geochemistry: Journal of African Earth Sciences, v. 58, p. 185-196.
- Abu-Alam, T.S., and Hamdy, M., 2014, Thermodynamic modelling of Sol Hamed serpentinite, South Eastern Desert of Egypt: implication for fluid interaction in the Arabian-Nubian Shield ophiolites: Journal of African Earth Sciences, v. 99, p. 7-23.
- Abzalov M.Z., 1998, Chromite-spinel in gabbro-wehrlite intrusions of the Pechenga area, Kola Peninsula, Russia: emphasis on alteration features: Lithos, v. 43, p. 109-134.
- Ahmed, A.H., 2013, Highly depleted harzburgite–dunite–chromitite complexes from the Neoproterozoic ophiolite, south Eastern Desert, Egypt: A possible recycled upper mantle lithosphere: Precambrian Research, v. 223, p. 173-192.
- Akaad, M.K., and Noweir, A.M., 1972, Some Aspects of the Serpentinites and their Associated Derivatives along Qift-Quesir Road, Eastern Desert: Annals of the Geological Survey of Egypt, v. 2, p. 251-270.
- Akbulut, M., Piskin, O., and Karayigit, A.I., 2006, The genesis of the carbonatized and silicified ultramafics known as listvenites: a case study from the Mihaliccik region (Eskisehir) NW Turkey: Geological Journal, v. 41, p. 557-580.
- Ali, K.A., Stern, R.J., Manton, W.I., Kimura, J.I., and Khamis, H.A., 2009, Geochemistry Nd isotopes and U-Pb SHRIMP zircon dating of Neoproterozoic volcanic rocks from the Central Eastern Desert of Egypt: New insight into the ~750 Ma crust-forming event: Precambrian Research, v. 171, p. 1-22.
- Ali-Bik, W. M., Taman, Z., El Kalioubi, B., and Abdel Wahab, W., 2012, Serpentinite-hosted talc–magnesite deposits of Wadi Barramiya area, Eastern Desert,

Egypt: Characteristics, petrogenesis and evolution: Journal of African Earth Sciences, v. 64, p. 77-89.

- Andréani, M., Mével, C., Boullier, A.M., and Escartin, J., 2007, Dynamic control on serpentine crystallisation in veins: constraints on hydration processes in oceanic peridotites: Geochemistry, Geophysics, Geosystems, v. 8 (2), p. 1-24.
- Andresen, A., Augland, L.E., Boghdady, G.Y., Lundmark, A.M., Elnady, O.M., and Hassan, M.A., 2010, Structural constraints on the evolution of the Meatiq gneiss domes (Egypt), East-African Orogen: Journal of African Earth Sciences, v. 57, p. 413-422.
- Andresen, A., El-Rus, M.M.A., Myhre, P.I., Boghdady, G.Y., and Corfu, F., 2009, U–Pb TIMS age constraints on the evolution of the Neoproterozoic Meatiq Gneiss Dome, Eastern Desert, Egypt: International Journal Earth Sciences, v. 98, p. 481-497.
- Arai, S., 1992, Chemistry of chromian spinel in volcanic rocks as a potential guide to magma chemistry: Mineralogical Magazine, 56, p. 173-184.
- Azer, M.K. 2013, Evolution and economic significance of listwaenites associated with Neoproterozoic ophiolites in south Eastern Desert, Egypt: Geologica Acta, v. 11, p. 113-128.
- Azer, M.K., 2014, Petrological studies of Neoproterozoic serpentinized ultramafics of the Nubian Shield: spinel compositions as evidence of the tectonic evolution of Egyptian ophiolites: Acta Geologica Polonica, v. 64, p. 113-127.
- Azer, M.K., and Stern, R.J., 2007, Neoproterozoic (835-720 Ma) serpentinites in the Eastern Desert, Egypt: Fragments of forearc mantle: The Journal of Geology, v. 115, p. 457-472.
- Bakor, A.R., Gass, I.G., and Neary, C.R., 1976, Jabal al Wask, northwest Saudi Arabia: an Eocambrian back-arc ophiolite: Earth and Planetary Science Letters, v. 30, p. 1-9.
- Barnes, I., O'Neil, J.R., Rapp, J.B., and White, D.E., 1973, Silicate-carbonate alteration of serpentine: wall rock alteration in mercury deposits of the California Coast Ranges: Economic Geology, v. 68, p. 388-398.
- Barnes, S.J., 2000, Chromite in Komatiites, II. Modifications during greenschist to mid-amphibolite facies metamorphism: Journal of Petrology, v. 41, p. 387-409.
- Basta, E.Z., and Abdel Kader, Z., 1969, The mineralogy of Egyptian serpentinites and talc-carbonates: Mineralogical Magazine, v. 37, p. 394-408.
- Bjerga, A., Konopásek, J., and Pedersen, R.B., 2015, Talc–carbonate alteration of ultramafic rocks within the Leka Ophiolite Complex, Central Norway: Lithos, v. 227, p. 21-36.
- Bodnar, R.J., 2003, Introduction to aqueous-electrolyte fluid inclusions. *in*: Samson, I., Anderson, A., and Marshall, D., eds., Fluid Inclusions: Analysis and Interpretation: Mineralogical Association of Canada, Short Course, v. 32, p. 81-99.
- Böhlke, J.K., 1989, Comparison of metasomatic reactions between a common CO_2-rich vein fluid and diverse wall rocks; intensive variables, mass transfers, and Au mineralization at Alleghany, California: Economic Geology, v. 84, p. 291-327.
- Boschi, C., Früh-Green, G.L., Delacour, A., Karson, J.A., and Kelley, D.S., 2006, Mass transfer nd fluid flow during detachment faulting and development of an

oceanic core complex, Atlantis Massif (MAR 30°N): Geochemistry, Geophysics, Geosystems, v. 7(1), p. 1-39.

- Botros, N.S., 2002, Metallogeny of gold in relation to the evolution of the Nubian Shield in Egypt: Ore Geology Reviews, v. 19, p. 137-164.
- Botros, N.S., 2004, A new classification of the gold deposits of Egypt: Ore Geology Reviews, v. 25, p. 1-37.
- Bregar, M., Bauernhofer, A., Pelz, K., Kloetzli, U., Fritz, H., and Neumayr, P., 2002, A late Neoproterozoic magmatic core complex in the Eastern Desert of Egypt: Emplacement of granitoids in a wrench-tectonic setting: Precambrian Research, v. 118, p. 59-82.
- Buisson, G., and LeBlanc, M., 1987, Gold in mantle peridotites from upper Proterozoic ophiolites in Arabia, Mali, and Morocco: Economic Geology, v. 82, p. 2091-2097.
- Cavanagh, B.J., 1979, Rb-Sr Geochronology of some Pre- Nubian Igneous Complexes of Central and Northeastern Sudan [Ph.D. thesis]: University of Leeds, 239 p.
- Chen, W.T., and Zhou, M., 2015, Mineralogical and geochemical constraints on mobilization and mineralization of rare Earth elements in the Lala Fe-Cu-(Mo, Ree) deposit, SW China: American Journal of Science, v. 315, p. 671-711.
- Coleman, R. G., 1977, Ophiolites: Berlin, Springer-Verlag, 229 p.
- Coleman, R.G., 1971, Petrologic and geophysical nature of serpentinites: Geological Society of America Bulletin. v. 82, p. 897-918.
- Debret, B., Andreani, A., Godard, M., Nicollet, C., Schwartz, S., and Lafay, R., 2013, Trace element behavior during serpentinization/de-serpentinization of an eclogitized oceanic lithosphere: A LA-ICPMS study of the Lanzo ultramafic massif (Western Alps): Chemical Geology, v. 357, p. 117-133.
- Deines, P., 1989, Stable isotope variations in carbonatites. *in*: Bell, K. (Ed.), Carbonatites: Genesis and evolution: Unwin Hyman, London, Boston, Sydney, Wellington, p. 301-359.
- Deines, P., 2002, The carbon isotope geochemistry of mantle xenoliths: Earth-Science Reviews, v. 58, p. 247-278.
- Demény, A., Ahijado, A., Casillas, R., and Vennemann, T.W., 1998, Crustal contamination and fluidrrock interaction in the carbonatites of Fuerteventura-Canary Islands, Spain: a C, O, H isotope study: Lithos v. 44, p. 101-115.
- Deschamps, F., Godard, M., Guillot, S., and Hattori, K.H., 2013. Geochemistry of subduction zone serpentinites: A review: Lithos, v. 178, p. 96-127.
- Deschamps, F., Godard, M., Guillot, S., Chauvel, C., Andreani, M., Hattori, K., Wunder, B., and France, L., 2012, Behavior of fluid-mobile elements in serpentines from abyssal to subduction environments: Examples from Cuba and Dominican Republic: Chemical Geology, 312-313, p. 93-117.
- Deschamps, F., Guillot, S., Godard, M., Andreani, M., and Hattori, K.H., 2011, Serpentinites act as sponges for fluid-mobile elements in abyssal and subduction zone environments: Terra Nova, v. 23, p. 171-178.

- Diamond, L.W., 2003, Systematics of H_2O inclusions. *in*: Samson, I., Anderson, A., Marshall, D., eds., Fluid Inclusions: Analysis and Interpretation: Mineralogical Association of Canada Short Course Series, v. 32, p. 55-79.
- Dick, H.J.B., and Bullen, T., 1984, Chromian spinel as a petrogenetic indicator in abyssal and Alpine-type peridotites and spatially associated lavas: Contributions to Mineralogy and Petrology, v. 86, p. 54-76.
- Droop, G.T.R., 1987, A general equation for estimating Fe^{3+} in ferromagnesian silicates and oxides from microprobe analysis, using stoichiometric criteria: Mineralogical Magazine, v. 51, p. 431-437.
- Eiler, J., 2001, Oxygen isotope variations of basaltic lavas and upper mantle rocks: Mineralogical Society of America, p. 319-364.
- El Bahariya, G.A., 2008, Geology, mineral chemistry and petrogenesis of Neoproterozoic metamorphosed ophiolitic ultramafics, Central Eastern Desert, Egypt: Implication for the classification and origin of the ophiolitic mélange: Egyptian Journal of Geology, v. 52, p. 55-81.
- El-Gaby, S., 2005, Integrated evolution and rock classification of the Pan-African belt in Egypt: First Symposium on the Classification of the Basement Complex of Egypt, p. 1-9.
- El-Gaby, S., El-Nady, O., and Khudeir, A., 1984, Tectonic evolution of the basement complex in the Central Eastern Desert of Egypt: Geologische Rundschau, v. 73, p. 1019-1036.
- El-Gaby, S., List, F.K., and Tehrani, R., 1988, Geology, evolution and metallogenesis of the Pan-African belt in Egypt. *in*: El Gaby, S., Greiling, R.O., eds., The Pan-African Belt of Northeast Africa and Adjacent Areas: Tectonic Evolution and Economic Aspects of a Late Proterozoic Orogen: Vieweg und Sohn, Braunschweig/Wiesbaden, p. 17-68.
- El-Sayed, M.M., Furnes, H., and Mohamed, F.H., 1999, Geochemical constraints on the tectonomagmatic evolution of the late Precambrian Fawakhir ophiolite, Central Eastern Desert, Egypt: Journal of African earth Sciences, v. 29, p. 515-533.
- Emam, A., and Zoheir, B., 2013, Au and Cr mobilization through metasomatism: Microchemical evidence from ore-bearing listvenite, South Eastern Desert of Egypt: Journal of Geochemical Exploration, v.125, p. 34-45.
- Engel, A.E.J., Dixon, T.H., and Stern, R.J., 1980, Late Precambrian evolution Afro-Arabian crust from ocean arc to craton: Geological Society of America Bulletin, v. 91, p. 699-706.
- Evans, B.W., 2004, The serpentinite multisystem revisited: Chrysotile is metastable: International Geology Review, v. 46, p. 479-506.
- Evans, B.W., 2010, Lizardite versus antigorite serpentinite: magnetite, hydrogen, life (?): Geology, v. 38, p. 879-882.
- Evans, B.W., and Guggenheim, S., 1988, Talc, pyrophyllite, and related minerals. *in*: S.W., Bailey, eds., Hydrous Phyllosilicates (exclusive of micas): Reviews in Mineralogy, v. 19, p. 225-294.
- Falk, E.S., and Kelemen, P.B., 2015, Geochemistry and petrology of listvenite in the Samail ophiolite, Sultanate of Oman: Complete carbonation of peridotite during ophiolite emplacement: Geochimica et Cosmochimica Acta, v. 160, p. 70-90.

- Fall, A., Tattitch, B. and Bodnar, R.J., 2011, Combined microthermometric and Raman spectroscopic technique to determine the salinity of H_2O-CO_2-NaCl fluid inclusions based on clathrate melting: Geochimica et Cosmochimica Acta, v. 75, p. 951-964.
- Farahat, E.S., 2008, Chrome-spinels in serpentinites and talc carbonates of the El Ideid-El Sodmein District, central Eastern Desert, Egypt: their metamorphism and petrogenetic implications. Chemie der Erde/Geochemistry, v. 68, p. 193-205.
- Farahat, E.S., El Mahallawi, M.M., Hoinkes, G., and Abdel Aal, A.Y., 2004, Continental back-arc basin origin of some ophiolities from the Eastern Desert of Egypt. Mineralogy and Petrology, v. 82, p. 81-104.
- Ferraris, C., and Lorand, J-P., 2015, Novodneprite ($AuPb_3$), anyuiite [$Au(Pb, Sb)_2$] and gold micro- and nano-inclusions within plastically deformed mantle-derived olivine from the Lherz peridotite (Pyrenees, France): a HRTEM–AEM–EELS study: Physics and Chemistry of Minerals, v. 42, p. 143-150.
- Fitches, W.R., Graham, R.H., Hussein, I.M., Ries, A.C., Shackleton, R.M., and Price, R.C., 1983, The late Proterozoic ophiolite of Sol Hamed, NE Sudan: Precambrian Research., v. 19, p. 385-411.
- Foster, R.P., 1991, Gold Metallogeny and Exploration. Blackie and Son, Glasgow, 432 p.
- Ghoneim, M. F., Salem, I. A., and Hamdy, M. M., 1999, On the petrogenesis of magnesite from Gebel El- Maiyit, central Eastern Desert, Egypt, *in* Fourth International Conference on the Geology of the Arab World, v. 1, p. 575-593.
- Ghoneim, M.F., Salem, I.A., and Hamdy, M.M., 2003, Origin of magnesite veins in serpentinites from Mount El-Rubshi and Mount El-Maiyit, Eastern Desert, Egypt: Archiwum Mineralogiczne, v. 54, p. 41-63.
- Gillis, K. M., and Meyer, P.S., 2001, Metasomatism of oceanic gabbros by late stage melts and hydrothermal fluids: Evidence from the rare earth element composition of amphiboles: Geochemistry, Geophysics, Geosystems, v. 2 (3).
- Griffis, R., 1972, Genesis of a magnesite deposit, Deloro Twp., Ontario: Economic Geology, v. 67, p. 63-71.
- Groves, D.I., Goldfarb, R.J., Gebre-Mariam, M., Hagemann, S.G., and Robert, F., 1998, Orogenic gold deposits: a proposed classification in the context of their crustal distribution and relationship to other gold deposit types: Ore Geology Review, v.13, p. 7- 27.
- Habib, M.E., Ahmed, A.A., and El Nady, O.M., 1985, Tectonic evolution of the Meatiq infrastructure, Central Eastern Desert, Egypt: Tectonics, 4 (7), p. 613-627.
- Halls C, and Zhao R. 1995, Listvenite and related rocks: perspectives on terminology and mineralogy with reference to an occurrence at Cregganbaun, Co. Mayo, Republic of Ireland: Mineralium Deposita, v. 30, p. 303-313.
- Halverson, G.P., Dudás, F. Ö., Maloof, A. C., and Bowring, S. A., 2007, Evolution of the $^{87}Sr/^{86}Sr$ composition of Neoproterozoic seawater: Palaeogeography, Palaeoclimatology, Palaeoecology, v. 256, p. 103-129.
- Hamdy, M.M., Harraz, Z.H., and Aly, A.G., 2013, Pan-African (intraplate and subduction-related?) metasomatism in the Fawakhir ophiolitic serpentinites, Central

Eastern Desert of Egypt: mineralogical and geochemical evidences: Arabian Journal of Geosciences, v. 6, p.13-33.

- Hansen, L.D., Dipple, G.M., Gordon, T.M., and Kellett, D.A., 2005, Carbonated serpentinite (listwanite) at Atlin, British Columbia: a geological analogue to carbon dioxide sequestration: The Canadian Mineralogist, v. 43, p. 225-239.
- Harraz, H.Z., 2000, A genetic model for a mesothermal Au deposit: evidence from fluid inclusions and stable isotopic studies at El Sid gold mine, Eastern Desert, Egypt: Journal of African Earth Sciences, v. 30, p. 267-282.
- Hattori, K.H., and Guillot, S., 2003, Volcanic fronts form as a consequence of serpentinite dehydration in the forearc mantle wedge: Geology, 31 (6), p. 525-528.
- Hattori, K.H., and Guillot, S., 2007, Geochemical character of serpentinites associated with high- to ultrahigh-pressure metamorphic rocks in the Alps, Cuba, and the Himalayas: recycling of elements in subduction zones: Geochemistry, Geophysics, Geosystems, 8 (9).
- Hussein, A.A., 1990, Mineral deposits. *in*: Said, R., (Ed.), The Geology of Egypt: Balkema, Rotterdam, p. 511-566.
- Irvine, T.N., 1965, Chromian spinel as petrogenetic indicator: Part 1. Theory: Canadian Journal of Earth Sciences. v. 2, p. 648-672.
- Ishii, T., Robinson, P. T., Maekawa, H., and Fiske, R., 1992, Petrological studies of peridotites from diapiric serpentinite seamounts in the Izu-Ogasawara-Marianaforearc, leg 125. *in* Proceedings of the Ocean Drilling Program, Scientific Results 125: College Station, TX, Ocean Drilling Program, p. 445-485.
- Johannes, W., 1969, An experimental investigation of the system $MgO–SiO_2–H_2O–CO_2$: American Journal of Science, v. 267, p. 1083-1104.
- Johnson, P.R., Kattan, F.H., and Al-Saleh, A.M., 2004, Neoproterozoic ophiolites in the Arabian Shield: Field relations and structure. In: Kusky, T.M. (Ed.), Precambrian Ophiolites and Related Rocks. *in*: Developments in Precambrian Geology, v. 13. Elsevier, Amsterdam, p. 129-162.
- Kelemen P. B., Matter J., Streit E. E., Rudge J. F., Curry W. B., and Bluztajn J., 2011, Rates and mechanisms of mineral carbonation in peridotite: natural processes and recipes for enhanced, in situ CO_2 capture and storage: Annual Review of Earth and Planetary Sciences, v. 39, p. 545-576.
- Kelemen, P. B., and Matter, J., 2008, In situ carbonation of peridotite for CO_2 storage: PNAS, 105(45), p. 17295-17300.
- Kerrick, D. M., and Caldeira, K., 1998, Metamorphic CO_2 degassing from orogenic belts: Chemical Geology, v. 145, p. 213-232.
- Khalil, A.E.S., and Azer, M.K., 2007, Supra-subduction affinity in the Neoproterozoic serpentinites in the Eastern Desert, Egypt: Evidence from mineral composition: Journal of African Earth Sciences, v. 49, p. 136-152.
- Khalil, A.E.S., Obeid M.A., and Azer, M.K., 2014, Serpentinized Peridotites at the North Part of the Wadi Allaqi District (Egypt): Implications for the Tectono-Magmatic Evolution of Fore-arc Crust: Acta Geologica Sinica, v. 88 (5), p. 1421-1436.
- Khalil, I.K., Helba, A.H., and Mücke, A., 2003, Genesis of the gold mineralization at the Dungash gold mine area, Eastern Desert, Egypt: a mineralogical-microchemical study: Journal of African Earth Sciences, v. 37, p. 111-122.

- Khedr, M.Z., and Arai, S., 2013, Origin of Neoproterozoic ophiolitic peridotites in south Eastern Desert, Egypt, constrained from primary mantle mineral chemistry: Mineralogy and Petrology, v. 107, p. 807-828.
- Klein, F., and Garrido, C.J., 2011, Thermodynamic constraints on mineral carbonation of serpentinized peridotite: Lithos, v. 126, p. 147-160.
- Klein, F., and McCollom, T.M., 2013, From serpentinization to carbonation: new insights from a CO_2 injection experiment: Earth and Planetary Science Letters, v. 379, p.137-145.
- Klemm, D., and Klemm, R., 2013, Gold and Gold Mining in Ancient Egypt and Nubia: Springer-Verlag Berlin Heidelberg, 649 p.
- Kodolányi, J., and Pettke, T., 2011, Loss of trace elements from serpentinites during fluid assisted transformation of chrysotile to antigorite—an example from Guatemala: Chemical Geology, v. 284, p. 351-362.
- Kröner, A., 1985, Ophiolites and the evolution of tectonic boundaries in the late Proterozoic Arabian-Nubian Shield of northeast Africa and Arabia: Precambrian Research, v. 27, p. 277-300.
- Kröner, A., Krüger, J., and Rashwan, A.A., 1994, Age and tectonic setting of granitoid gneisses in the Eastern Desert of Egypt and south-west Sinai. Geologische Rundschau. v. 83, p. 502-513.
- Kröner, A., Todt, W., Hussein, I.M., Manour, M., and Rashwan, A.A., 1992, Dating of late Proterozoic ophiolites in Egypt and the Sudan using the single grain zircon evaporation technique: Precambrian Research, v. 59, p. 15-32.
- Lackner, K. S., Wendt, C. H., Butt, D. P., Joyce, E. L., and Sharp, D. H., 1995, Carbon dioxide disposal in carbonate minerals: Energy, v. 20, p. 1153–1170.
- Lasaga, A.C., Rye, D.M., Lüttge, A., and Bolton, E.W., 2001, Calculation of fluid fluxes in Earth's crust: Geochimica et Cosmochimica Acta, v. 65, p. 1161-1185.
- Loizenbauer, J., Wallbrecher, E., Fritz, H., Neymayr, P., Khudeir, A.A., and Kloetzli, U., 2001, Structural geology, single zircon ages and fluid inclusion studies of the Meatiq metamorphic core complex: implications for Neoproterozoic tectonics in the Eastern Desert of Egypt: Precambrian Research, v. 110, p. 357-383.
- McDonough, W.F., and Sun, S.S., 1995, Composition of the Earth: Chemical Geology, v. 120, p. 223-253.
- Mellini, M., Trommsdorff, V., and Compagnoni, R., 1987, Antigorite polysomatism: behavior during progressive metamorphism: Contributions to Mineralogy and Petrology, v. 97, p. 147-155.
- Neumayr, P., Hoinkes, G., Puhl, J., Mogessie, A., and Khudeir, A.A., 1998, The Meatiq dome (Eastern Desert, Egypt) a Precambrian metamorphic core complex: petrological and geological evidence: Journal of Metamorphic Geology, v. 16, p. 259-279.
- Neumayr, P., Mogessie, A., Hoinkes, G., and Puhl, J., 1996, Geological Setting of the Meatiq metamorphic core complex in the Eastern Desert of Egypt based on amphibolite geochemistry: Journal of African Earth Science, v. 23, p. 331-345.
- O'Hanley, D.S., 1996, Serpentinites: records of tectonic and petrological history: Oxford Monographs in Geology and Geophysics, v. 34, 277 p.

- Osman, A., 1995, The mode of occurrence of gold-bearing listvenite at El Barramiya gold mine, Eastern Desert, Egypt. Middle East Research Centre, Ain Shams University: Earth Sciences Series, v. 9, p. 93-103.
- Pallister, J.S., Stacey, J.S., Fischer, L.B., and Premo, W.R., 1988, Precambrian ophiolites of Arabia: Geologic settings, U-Pb geochronology, Pb-isotope characteristics, and implications for continental accretion: Precambrian Research, v. 38, p. 1-54.
- Phillips G.N., and Evans K.A., 2004, Role of CO_2 in the formation of gold deposits: Nature, v. 429, p. 860-863.
- Pitcairn, I.K., Craw, D., and Teagle, D.A.H., 2014, The gold conveyor belt: large-scale gold mobility in an active orogeny: Ore Geology Reviews, v. 62, p. 129-142.
- Pitcairn, K.I., Warwick, E.P., Milton J.A., and Teagle, A.H.D., 2006, Method for Ultra-Low-Level Analysis of Gold in Rocks: Analytical Chemistry, v. 78, p.1290-1295.
- Reischmann, T., 1986, Geoiogie und Genese Spriitproterozoischer Vulkanite der Red Sea Hills, Sudan [Ph.D. thesis]: Johannes Gutenberg Universith't Mainz, 202 p.
- Ries, A. C., Shackleton, R. M., Graham, R. H., and Fitches, W. R., 1983, Pan-African structures, ophiolites and melange in the Eastern Desert of Egypt: A tranverse at 26°N: Geological Society of London Journal, v. 140, p. 75-95.
- Robinson, P.T., Malpas, J., Zhou, M.F., Ash, C., Yang, J.S., and Bai, W.J., 2005, Geochemistry and origin of listwanites in the Sartohay and Luobnsa ophiolites, China: International Geology Review, v. 47, p. 177-202.
- Roedder, E., 1984, Fluid inclusions. Mineralogical Society of America: Reviews in Mineralogy and Geochemistry, v. 12, 644 p.
- Rosenbaum, J., and Sheppard, S.M.F., 1986, An isotopic study of siderites, dolomites and ankerites at high temperatures: Geochimica et Cosmochimica Acta, v. 50, p. 1147-1150.
- Salters, V.J.M., and Stracke, A., 2004, Composition of the depleted mantle: Geochemistry, Geophysics, Geosystems, v. 5, Q05B07, 27p.
- Scambelluri, M., Müntener, O., Hermann, J., Piccardo, G.B. and Trommsdorff, V., 1995, Subduction of water into the mantle: history of an alpine peridotite: Geology, v. 23, p. 459-462.
- Schandal, E.S. and Naldrett, A.J. 1992, CO_2 metasomatism of serpentinites, south of Timmins, Ontario: The Canadian Mineralogist: v. 30, p. 93-108.
- Schwartz, S., Guillot,S., Reynard, B., Lafay, R., Debret, b., Nicollet, C., Lanari, P., and Auzende, A., 2013, Pressure–temperature estimates of the lizardite/antigorite transition in high pressure serpentinites: Lithos, v. 178, p. 197-210.
- Seifritz, W., 1990, CO_2 disposal by means of silicates: Nature, v. 345, p. 486-490.
- Shepherd, T.J., Rankin, A.H. and Alderton, D.H.M., 1985, A practical guide to fluid inclusion studies: Blackie, Glasgow. 239 p.
- Skelton, A., 2011, Flux rates for water and carbon during greenschist facies metamorphism: Geology, v. 39, p. 43-46.
- Stern, R,J., Johanson, P.R., Kroner, A., and Yibas, B., 2004, Neoproterozoic ophiolites of the Arabian–Nubian Shield. In: Kusky TM (ed) Precambrian ophiolites

and related rocks. Developments in Precambrian geology: Elsevier, Amsterdam, v.13, p. 95-28.

- Stern, R.J. and Hedge, C.E., 1985, Geochronologic and isotopic constraints on Late Precambrian crustal evolution in the Eastern Desert of Egypt: American Journal of Science, v. 285, p. 97-127.
- Stern, R.J., 1994. Arc Assembly and continental collision in the Neoproterozoic East African Orogen: Implications for the assembly of Gondwanaland: Annual Reviews of Earth and Planetary, Sciences, v. 22, p. 319-351.
- Stern, R.J., 2002, Crustal evolution in the East African Orogen: a neodymium isotopic perspective: Journal of African Earth Sciences, v. 34, p. 109-117.
- Stern, R.J., and Gwinn, C.J., 1990, Origin of late Precambrian intrusive carbonates, Eastern Desert of Egypt and Sudan: C, O and Sr isotopic evidence: Precambrian Research, v. 46, p. 259-272.
- Sturchio, N.C., Sultan, M., and Batiza, R., 1983, Geology and origin of Meatiq dome, Egypt: A Precambrian metamorphic core complex? Geology, v. 11, p. 72-76.
- Takla, M.A., and Surour, A.A., 1996, On the occurrence of Ni-sulphides and arsenides in some Egyptian serpentinites: Egyptian Minerals, v. 8, p. 1-18.
- Taylor, H.P., Frechen, J. and Degens, E.T., 1967, Oxygen and carbon isotope studies of carbonatites from the Laacher See district, West Germany and the Alno district, Sweden: Geochimica et Cosmochimica Acta, v. 31, p. 407-430.
- Trommsdorff, V., Sanchez-Vizcaino, V.L., Gomez-Pugnaire, M.T., and Muntener, O., 1998, High pressure breakdown of antigorite to spinifex-textured olivine and orthopyroxene, SE Spain: Contributions to Mineralogy and Petrology, v. 132, p. 139-148.
- Tsay, A., Zajacz, Z., and Sanchez-Valle, C., 2014, Efficient mobilization and fractionation of rare-earth elements by aqueous fluids upon slab dehydration: Earth and Planetary Science Letters, v. 398, p. 101-112.
- Tsikouras, B., Karipi, S., Grammatikopoulos, T.A., and Hatzipanagiotou, K., 2006, Listwaenite evolution in the ophiolite melange of Iti Mountain (continental Central Greece): European Journal of Mineralogy, v. 18, p. 243-255.
- Uçurum, A., 2000, Listwaenites in Turkey: Perspectives on formation and precious metal concentration with reference to occurrences in East-Central Anatolia: Ofioliti, v. 25, p. 15-29.
- Van den Kerkhof, A., and Thiéry, R., 2001, Carbonic Inclusions: Lithos, v. 55, p. 49-68.
- Vils, F., Müntener, O., Kalt, A., and Ludwig, T., 2011, Implications of the serpentine phase transition on the behaviour of beryllium and lithium-boron of subducted ultramafics rocks: Geochimica et Cosmochimica Acta, v. 75, p. 1249-1271.
- Wallbrecher, E., Fritz, H.E., Khudier, A.A., and Farahad, F., 1993, Kinematics of Panafrican thrusting and extension in Egypt. *in*: Thorweihe, U., Schandelmeier, H., eds., Geoscientific Research in Northeast Africa, Proceedings of the international conference on geoscientific research in Northeast Africa. Balkema, Rotterdam, p. 27-30.

- Will, T. M., Powell, R., Holland, T. J. B., Guiraud, M., 1990, Calculated greenschist facies mineral equilibria in the system $CaO–FeO–MgO–Al_2O_3–SiO_2–CO_2–H_2O$: Contributions to Mineralogy and Petrology, v. 104, p. 353-368.
- Zimmer, M., Kröner, A., Jochum, K.P., Reischmann, T., and Todt, W., 1995, The Gabal Gerf complex: A Precambrian N-MORB ophiolite in the Nubian Shield, NE Africa: Chemical Geology, v. 123, p. 29-51.
- Zoheir, B., 2012, Lode-gold mineralization in convergent wrench structures: Examples from South Eastern Desert, Egypt: Journal of Geochemical Exploration, v. 114, 82-97.
- Zoheir, B., and Moritz, R. 2014, Fluid evolution in the El-Sid gold deposit, Eastern Desert, Egypt. *in*: Garofalo, P.S., Ridley, J.R., eds., Gold-transporting hydrothermal fluids in the Earth's crust: Geological Society, London, Special Publications, 402 p.
- Zoheir, B.A., and Lehmann, B., 2011, Listvenite-lode association at the Barramiya gold mine, Eastern Desert, Egypt: Ore Geology Reviews, v. 39, p. 101-115.

Figure captions

Figure 1. Simplified geological map showing the extent of the ANS (inset), the distribution of ophiolitic bodies and selected Au deposits in the Egyptian segment of ANS.

Figure 2. (a) General geological map of Neoproterozoic basement in the Meatiq area (after El-Gaby et al. 1984; Loizenbauer et al. 2001; Andresen et al. 2009, 2010; Abd El-Rahman et al. 2010), showing important lithologies, sample localities and strike-slip structures. (b) Inset shows the location of the Meatiq area in the CED, Egypt. (c) Schematic cross-section across Meatiq Gneiss Dome showing the relationship between the Meatiq Dome lithologies, the surrounding ophiolitic rocks, Hammamat clastics and Dokhan Volcanics. The ages are from Andresen et al. (2009).

Figure 3. Field photographs of serpentinites and talc-rich rocks in the study area. (a) Mesh-textured Lz-serpentinite from locality A with visible chrysotile veinlets. (b) Lz-serpentinite exposures in locality A showing cross-cutting veinlets of fibrous chrysotile (Ctl). (c) Atg-serpentinite showing relict mesh textures from locality B. (d) Exposures of altered Atg-serpentinite from locality B. The pale layers are highly sheared talc-rich rocks. Location of photo is shown in Figure 4. (e) A carbonate (Cb) and quartz (Qz) vein hosted within sheared talc-rich rocks from locality B. Location of photo is shown in Figure 4. (f) The talc quarry

from locality B showing cut surfaces of Atg-serpentinite. Location of photo is shown in Figure 4 (g) talc-rich rocks in a shear zone with sharp contacts to altered serpentinites in locality C. (h) An exposure of serpentinite with pale coloured shear-hosted talc-rich rocks from locality C. Sharp contact with shear zone to altered serpentinite control the location of the talc-rich rocks. (i) Sheared talc-schist between more coherent bodies of Atg-serpentinite from Locality C. (j) The view north from locality C showing extensive outcrop of shear-hosted listvenitic rocks within serpentinite.

Figure 4. Simplified geological map of locality B showing patches of talc-rich rocks within antigorite serpentinite, the location of the talc quarry, sampling localities, and the position where photos in figure 3 were taken. The dotted line leading to the quarry is a road.

Figure 5. Photomicrographs (a, b, d, e, g, h) and back-scattered electron (BSE) images (c, f and i) of the investigated ophiolitic rocks in Meatiq area. (a) Lz-serpentinite with mesh texture and lizardite hourglass pseudomorphs after olivine together with late chrysotile veinlets, locality A-sample Me21. (b) Late chrysotile (Ctl) veinlets invaded by diffusive dolomite (Dol), locality A-sample Me22. (c) Slightly altered Cr-spinel with a very thin narrow Cr-rich magnetite (Cr-Mag) rim, locality A-sample Me21. (d) Antigorite flakes are intergrown with magnesite (Mgs) and minor talc (Tlc) in Atg-serpentinite, locality B-sample Me5. (e) Atg-serpentinite invaded by vein of talc and magnesite, locality B-sample Me9. (f) Cr-spinel alteration to ferritchromite (Fe-Chr) and Cr-rich magnetite (light-grey) with preservation of unaltered chromite (Chr, dark-grey) in the core, locality B-sample Me5. (g) Dynamically crystallized tremolite (Tr) in highly foliated talc-schist during progressive deformation, locality C-sample Me15. (h) Talc-schist rock with long anthophyllite fibres and ferritchromite embedded in chromium clinochlore (Clc), locality C-sample Me17. (i) Cataclastic texture in altered Cr-spinel (Fe-Chr) grain indicates intensive shearing in fault zones locality C-sample Me1.

Figure 6. Three-dimensional representation of LOI and major elements, showing their distribution in two varieties of serpentinites and talc-rich rocks in the study area. Compositions are recalculated on a volatile free basis.

Figure 7. Harker-type diagrams showing variations in compatible trace elements of different serpentinites and talc-rich rocks. Au values plotted from two sets of serpentinites analyses. Question marks indicate values below detection limit.

Figure 8. Trace element patterns for two varieties of serpentinites, talc-rich rocks and carbonate veins. (a) Compositions of Lz- and Atg-serpentinites. Primitive mantle normalizing values are after McDonough and Sun (1995). (b) and (c) REE compositions of two varieties of serpentinites, carbonate veins, and talc-rich rocks, respectively. (d) Average compositions of Lz- and Atg-serpentinites, talc-rich rocks and carbonate veins. Chondrite-normalizing values after McDonough and Sun (1995).

Figure 9. Plots of O, C and Sr isotope data for Meatiq serpentinites and carbonate veins. Data for Central Eastern Desert (CED) and sedimentary carbonates are adopted from Stern and Gwinn (1990). Field of Neoproterozoic mantle-derived carbonates (dashed-line boxes) is taken from C-isotopic data of Taylor et al. (1967) and Deines (1989), and Sr-isotopic data for Egyptian basement rocks (solid-line box) is from Stern and Hedge (1985). Data for Oman listvenites are adopted from Falk and Kelemen (2015). (a) $\delta^{13}C$ vs. $^{87}Sr/^{86}Sr$ at ~ 600Ma; (b) $\delta^{13}C$ vs. $\delta^{18}O$ from the same samples, with similar fields displayed; (c) $\delta^{18}O$ vs. $^{87}Sr/^{86}Sr$ at ~ 600Ma with similar reference fields outlined.

Figure 10. Photomicrographs of typical fluid inclusions in quartz/carbonate veins: (a) type-I, aqueous inclusion (LH_2O+VH_2O). (b) Type-II, aqueous-carbonic ($LH_2O+LCO_2+VCO_2$). (c) Type-III, carbonic inclusion (LCO_2+VCO_2). (d) Trails of secondary inclusion crossing grain boundaries. (e) Elongation and necking down of inclusions in the direction of the trails. (f) Fluid inclusion with shear sense in magnesite vein (Me9).

Figure 11. (a) Ternary plot of Al_2O_3-MgO-CaO for bulk rock compositions of Meatiq serpentinites compared with peridotites from other tectonic settings (after Coleman 1977). (b) CaO vs. Al_2O_3 diagram comparing Meatiq serpentinites with peridotites from other tectonic settings (after Ishii et al. 1992). (c) Cr# versus Mg# for the analyzed spinel cores in Meatiq serpentinites. Data for different tectonic environments were compiled from the literature following Stern et al. (2004). The field for core of Cr-spinel compositions occurring in some of the serpentinites from the Central Eastern Desert of Egypt (CED) is also shown (Azer and Stern 2007; Hamdy et al. 2013; Azer 2014). MORB = mid-ocean ridge basalt. Compositions are recalculated on a volatile free basis.

Figure 12. P-T diagram based on intersecting isochores of aqueous fluid inclusions with homogenization of 225˚C and a salinity of 5 mass% NaCl and CO_2 inclusions with molar volumes of 65 and 90 cm^3/mol. The diagram shows estimated trapping condition for fluid inclusions in carbonate veins at 270˚C-300˚C and 0.7-1.1 kbar.

Figure 13. Sr composition of carbonate veins and altered serpentinites in the Meatiq study area compared to values from Neoproterozoic intrusive carbonates from Eastern Desert of Egypt. The ages of emplacement for the intrusive carbonates are estimated from the age of the surrounding basement units (after Cavanagh 1979; Stern and Hedge 1985; Reischmann 1986; Stern and Gwinn 1990). Field of initial $^{87}Sr/^{86}Sr$ for Egyptian basement igneous rocks is shown after Stern and Hedge (1985); this field represents an upper limit for the isotopic composition of Sr in the depleted mantle beneath northeast Africa at that time. Fields of initial $^{87}Sr/^{86}Sr$ for CED carbonate veins is shown after Stern and Gwinn (1990). Isotopic composition of Neoproterozoic seawater is also shown after Halverson et al. (2007).

Figure 14. Back-scattered electron (BSE) images showing different mineral phases in serpentinites and carbonate veins. (a) Ni-sulphide (i.e. pentlandite-Pn) in Lz-serpentinites

converted to Ni-rich magnetite (Ni-Mag) in the rims (Me23). (b) Total conversion of pentlandite to Ni-rich magnetite in Atg-serpentinites (Me7). Figures (c) and (d) show REE-bearing minerals (Zircon-Zr, apatite-Ap, Monazite-Mnz and rutile-Rt) in a carbonate vein (Me12).

Figure 15. Plots of concentrations of fluid-mobile elements (Li, As, S, Sb, Pb, U, Ba, Sr and Cs) and Au in two serpentine phases from the Meatiq study area. Values of primitive mantle after McDonough and Sun (1995) and depleted mantle after Salters and Stracke (2004) are also reported (thick and dashed black lines). Grey boxes represent the ranges between primitive and depleted mantle. Au values plotted from two sets of serpentinites analyses.

Figure 16. Schematic cross section illustrating the characteristics and evolution of the different serpentinite and listvenitic rocks and the tectonic setting where, based on the alteration assemblages and fluid inclusion compositions, these rocks formed. The principal transfer of fluid-mobile elements is also noted, as well as geochemical signature of fluids released during dehydration of serpentinites, "antigorite formation" due to the prograde metamorphism and later "listvenitization". Mineral abbreviations as in Fig. 5.

Table 1 Chemical composition of different rock types and carbonate veins in the study area

Lithology	Atg-serpentinites					Lz-serpentinites				Talc-rich rocks				Carbonate veins		
sample	Me5	Me6	Me7	ME8	Me9	Me21	Me22	Me23	Me24	Me1	Me14	Me15	Me17	Me2	Me12	Me28
SiO_2 (wt.%)	40.26	36.97	34.37	37.12	32.75	40.43	39.29	38.6	37.76	55.5	59.23	58.95	57.92	n.d.	n.d.	n.d.
Al_2O_3	0.48	0.51	0.31	0.51	0.12	0.51	0.5	0.48	0.55	1.66	1	0.38	1.57	n.d.	n.d.	n.d.
FeO(T)	7.63	9.07	7.36	6.3	5.86	6.78	7.28	7.49	7.81	7.6	4.8	5.33	7.98	n.d.	n.d.	n.d.
MnO	0.07	0.09	0.14	0.09	0.11	0.07	0.08	0.08	0.10	0.16	0.06	0.12	0.12	n.d.	n.d.	n.d.
MgO	38.43	38.52	39.11	38.81	39.18	38.22	37.99	37.47	37.68	20.16	27.08	22.52	23.36	n.d.	n.d.	n.d.
CaO	0.02	0.02	0.03	0.02	0.05	0.27	0.76	1.11	1.13	12.6	2.71	11.24	6.55	n.d.	n.d.	n.d.
Na_2O	< 0.01	0.01	< 0.01	< 0.01	< 0.01	< 0.01	< 0.01	0.01	< 0.01	0.08	0.03	0.05	0.09	n.d.	n.d.	n.d.
K_2O	< 0.01	< 0.01	< 0.01	< 0.01	< 0.01	< 0.01	< 0.01	< 0.01	< 0.01	0.01	< 0.01	< 0.01	< 0.01	n.d.	n.d.	n.d.
TiO_2	0.002	0.001	0.002	0.001	0.001	0.002	0.001	0.003	0.002	0.025	0.006	0.014	0.033	n.d.	n.d.	n.d.
P_2O_5	< 0.01	< 0.01	< 0.01	< 0.01	< 0.01	< 0.01	< 0.01	0.02	< 0.01	< 0.01	< 0.01	< 0.01	< 0.01	n.d.	n.d.	n.d.
L.O.I.	12.55	15.28	18.34	15.06	20.84	13.19	13.55	13.85	14.19	2.1	4.1	2.34	3.13	_	_	_
Total	99.43	100.5	99.67	97.92	98.92	99.48	99.46	99.11	99.22	99.89	99.01	101	100.8	n.d.	n.d.	n.d.
Sc (ppm)	7.8	8.7	8.3	8.5	2.6	7.2	6.9	6.2	5.9	5	5	5	24	3.9	6.8	3.3
V	29.4	34.5	23.9	29.7	12.5	28.1	36.7	49.8	20.2	53	27	47	71	3.0	0.16	0.08
Cr	2526	3145	2191	2651	951	1220	1924	2016	1782	1670	1990	230	1830	7.5	3.6	3.3
Co	93.3	102	123	99.1	99.6	110.6	101.5	92	92.9	74	75	46	60	0.74	12.5	9.5
Ni	2286	2173	2310	2344	2428	2516	2255	1951	2147	1600	2020	619	371	4.2	33	33.6
Rb	0.03	0.03	0.02	0.03	0.01	0.11	0.09	0.12	0.03	b.d.l.	b.d.l.	b.d.l.	b.d.l.	0.04	0.01	0.001
Sr	0.23	0.42	0.31	0.40	0.45	5.82	18.5	69.8	56.4	25	b.d.l.	5.0	8.0	1135	503	2365
Y	0.05	0.04	0.01	0.03	0.02	0.52	0.71	2.1	0.04	0.6	b.d.l.	0.5	0.9	20.9	46.9	18.1
Nb	0.03	0.03	0.1	0.03	0.04	0.03	0.03	0.07	0.01	b.d.l.	b.d.l.	b.d.l.	b.d.l.	0.04	0.02	0.02
Sb	1.1	0.76	1.1	0.92	0.72	0.78	0.71	0.52	0.26	b.d.l.	b.d.l.	b.d.l.	b.d.l.	n.d.	n.d.	n.d.
As	9.3	6.2	6.4	8.0	6.1	46.1	34.5	16.8	4.1	66.0	b.d.l.	b.d.l.	b.d.l.	n.d.	n.d.	n.d.
S	b.d.l.	30	20	b.d.l.	b.d.l.	380	280	730	400	b.d.l.	20	10	10	n.d.	n.d.	n.d.
Au (ppb)	7.7	1.4	1.8	1.8	0.86	11.2	10.3	3.7	3.8	1.0	0.30	1.4	0.24	n.d.	n.d.	n.d.
Au**	4.3	1.6	1.4	1.3	0.85	12.6	12.4	4.9	4.6	n.d.	n.d.	n.d.	n.d.	n.d.	n.d.	n.d.
Li	479	430	413	407	567	5697	5027	4533	573	n.d.	n.d.	n.d.	n.d.	489	613	534
Cs	157	63.4	65.4	83.2	18.9	44.4	32.3	44.9	2.7	b.d.l.	b.d.l.	b.d.l.	b.d.l.	3.5	2.7	6.5
Ba	b.d.l.	226	341	168	522	646	1512	2483	2174	3	b.d.l.	b.d.l.	b.d.l.	4781	973	1573
La	17.0	16.1	5.3	12.5	13.7	530	589	566	65.8	170	160	220	340	16410	4711	2358
Ce	39.1	31.4	8.7	24.6	23.7	1182	1274	1181	30.9	260	270	420	670	33730	15330	7715
Pr	3.6	3.4	0.42	2.8	2.0	166	180	161	0.50	60	30	50	80	4324	2631	1324
Nd	18.8	13.7	1.9	9.1	9.7	656	713	655	1.1	200	b.d.l.	b.d.l.	240	18340	14190	7088
Sm	4.5	3.1	0.01	1.9	0.91	104	119	118	b.d.l.	30	b.d.l.	b.d.l.	40	3939	4888	2489
Eu	8.1	4.7	2.8	4.1	5.9	26.7	28.8	31.6	16.3	73	b.d.l.	6	38	1464	1538	956
Gd	5.3	4.5	b.d.l.	1.4	1.4	101	118	136	0.31	90	b.d.l.	40	100	3783	6790	3235
Tb	0.76	0.95	0.06	0.44	0.35	14.5	16.4	23.5	0.24	10	b.d.l.	b.d.l.	20	508	1132	507
Dy	6.1	6.9	0.97	3.0	1.8	80.6	96.9	185	3.2	70	30	60	110	2663	7270	3026
Ho	1.3	1.4	0.29	0.70	0.35	14.6	18.5	52.3	1.2	20	b.d.l.	10	30	491	1531	577
Er	4.9	5.7	2.2	3.9	2.0	26.4	45.1	184	6.3	50	30	50	90	1253	4295	1482
Tm	1.1	1.4	0.69	1.0	0.40	2.6	5.7	27.9	1.7	6	b.d.l.	9	14	169	591	195
Yb	11	12.3	8.7	8.6	5.9	14.8	35.7	168	15.0	30	20	80	100	1046	3720	1159
Lu	2.4	2.9	2.6	2.4	1.1	2.6	4.4	22.8	3.7	3	3	16	17	140	524	156
Hf	5.0	7.7	3.7	7.6	2.0	8.8	3.7	7.0	3.6	b.d.l.	b.d.l.	b.d.l.	b.d.l.	8.1	20	8.3
Ta	8.0	4.9	3.0	9.0	2.1	3.3	3.9	5.4	4.2	b.d.l.	b.d.l.	b.d.l.	b.d.l.	3.1	7.8	2.8
Pb	52.8	44.4	41.5	43.4	28.8	110	97.2	103	440	4000	3000	b.d.l.	4000	882	3176	4908
Th	2.9	2.2	1.8	1.4	1.0	3.2	5.7	14.5	1.8	b.d.l.	b.d.l.	b.d.l.	b.d.l.	18.9	8.8	5.9
U	46.7	39.1	0.87	1.5	5.7	255	375	504	4.0	40	20	30	30	14.9	0.74	0.44
Eu/Eu*	5.1	3.9	_	7.7	15.8	0.80	0.74	0.76	_	4.3	_	_	1.8	1.2	0.82	1.0
(La/Sm)N	2.4	3.3	246	4.3	9.7	3.3	3.2	3.1	_	3.7	_	_	5.5	2.7	0.62	0.61
(La/Yb)N	1.1	0.94	0.44	1.0	1.7	25.8	11.8	2.4	3.2	4.1	5.7	2.0	2.4	11.3	0.91	1.5
(La/Lu)N	0.77	0.60	0.22	0.56	1.3	22.1	14.4	2.7	1.9	6.1	5.7	1.5	2.1	12.6	1.0	1.6
(Tb/Yb)N	0.31	0.35	0.03	0.23	0.27	4.5	2.1	0.64	0.07	1.5	_	_	0.91	2.2	1.4	2.0
Total REE (ppm)	0.12	0.11	0.03	0.08	0.07	2.9	3.2	3.5	0.15	1.1	0.54	0.96	1.9	88.3	69.1	32.3

From Sc to S in ppm, from Au to U in ppb, n.d. (not determined), b.d.l. (below detection limit), Au** values for the second group of the same serpentinites.

Table 2 Geochemical and isotopic data, Meatiq study area

Sample	Concentrations (ppm)[a]		$^{87}Rb/^{86}Sr$	$^{87}Sr/^{86}Sr$	$(^{87}Sr/^{86}Sr)_{600}$[b]	$\delta^{18}O$ (SMOW)	$\delta^{13}C$ (PDB)
	Rb	Sr					
Atg-serpentinites							
Me05	0.028	0.23	0.352	0.70697±17	0.70396	11.0	-5.4
Me06	0.025	0.42				10.6	-5.9
Me07	0.022	0.31				11.0	-5.6
Me08	0.031	0.40	0.226	0.70779±15	0.70585	10.3	-5.6
Me09	0.009	0.45				11.5	-5.3
Lz-serpentinites							
Me21	0.11	5.82	0.054	0.70669±16	0.70622	15.1	-4.2
Me22	0.093	18.49	0.014	0.70461±13	0.70448	14.0	-4.1
Me23	0.117	69.75	0.005	0.70432±16	0.70428	12.3	-4.2
Me24	0.033	56.37	0.002	0.70422±14	0.70421	13.7	-4.2
Carbonate veins							
Me02	0.04	1135	0.0001	0.70344±12	0.70344	6.4	-8.1
Me12	0.005	503	0.00003	0.70281±13	0.7028	9.4	-6.8
Me28	0.001	2365	0.000001	0.70293±13	0.70293	10.5	-6.8

[a] Blank-corrected concentrations.

[b] Isotopic composition at 600 Ma.

Table 3 Microthermometric data of fluid inclusions from the Meatiq study area

Sample	Fluid inclusion Type	$TmCO_2$ (°C)	Tm ice (°C)	Tm,cla (°C)	$ThCO_2$ (°C)	Salinity (mass% NaCl)	Th total (°C)
	type-I						
Dol-Me2	Mg-Na-Cl-H_20		-2.6 to 0.0			0.0 to 4.3	239 to 265
Dol-Me2	Ca-Na-Cl-H_2O		-16.4 to -4.0			6.4 to 16.9*	225 to 383
Dol-Me2	Mg-Na-Cl-H_20 secondary		-1.3 to 0.0			0.0 to 2.2	161 to 255
Qz-Me3	Mg-Na-Cl-H_20		-3.5 to -0.1			0.2 to 5.7*	225 to 266
Qz-Me3	Mg-Na-Cl-H_20 secondary		-3.5 to -0.1			0.2 to 5.7	177 to 234
Mgs-Me9	Mg-Na-Cl-H_20		-2.4 to -0.5			0.9 to 5.0	231 to 335
Dol-Me12	Mg-Na-Cl-H_20		-2.9 to -0.8			1.4 to 4.8	253 to 302
Dol-Me28	Mg-Na-Cl-H_20		-3.3 to -1.0			1.7 to 5.5	262 to 315
	type-II						
Qz-Me3	CO_2±(CH_4/N_2)-H_2O-NaCl	-57.7 to -56.6		7.7 to 9.5	26.8 to 28.0	1.0 to 4.7*	305 to 331 324 to 365 (g)
Dol-Me12	CO_2±(CH_4/N_2)-H_2O-NaCl	n.d.		7.5 to 9.8		0.2 to 4.9	252 to 276
Dol-Me28	CO_2±(CH_4/N_2)-H_2O-NaCl	-57.3 to -56.6		6.6 to 10.0	26.8 to 29.2	0.0 to 6.8	242 to 331
	type-III						
Qz-Me3	CO_2±(CH_4/N_2)	-57.3 to -56.6			26.8 to 29.5		

Tm,CO_2 = melting of the CO_2; Tm,cla = melting of CO_2 hydrate; Th,CO_2 = homogenization of the CO_2 phases to liquid (l); Tm,ice = final melting of ice; Salinity = wt.% NaCl calculated from Tm,ice or Tm,cla; Th,total = total homogenization to the liquid phase or gas phase (g); Tc = critical homogenization temperature; Dol = dolomite; Qz = quartz; Mgs = magnesite; n.d. (not detected). *mass % ($NaCl+CaCl_2$) eq.

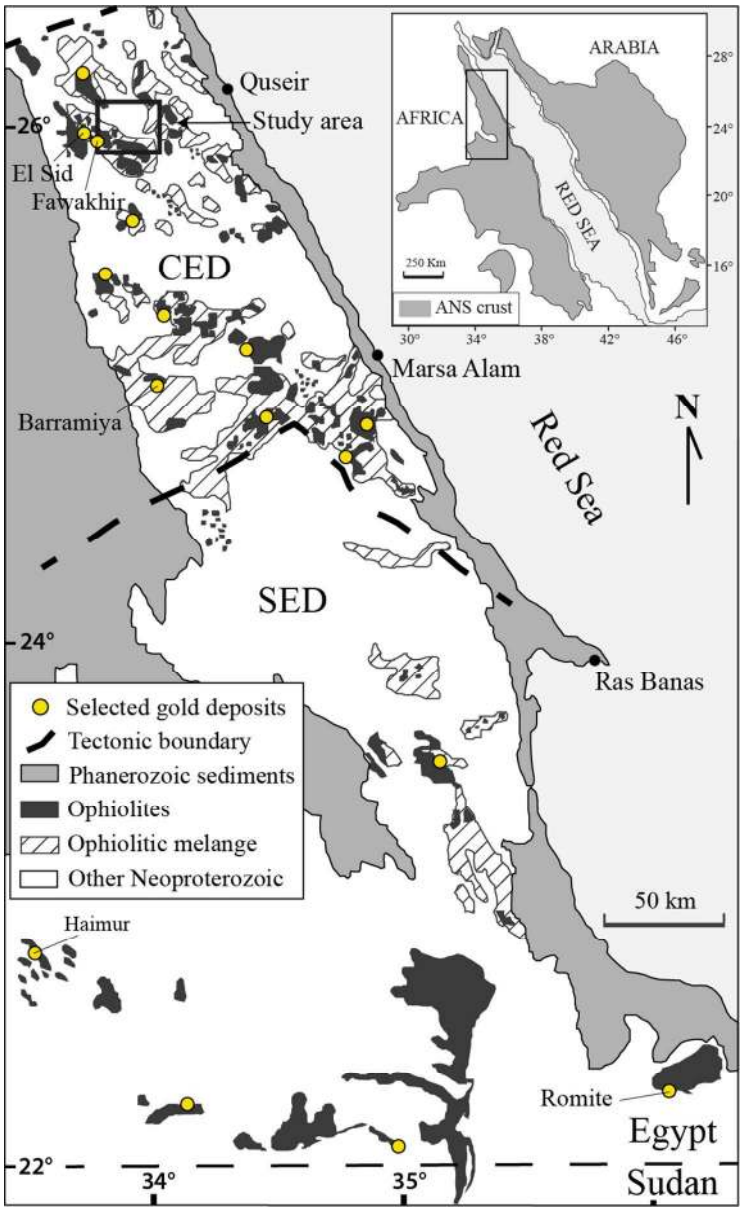

84x137mm (300 x 300 DPI)

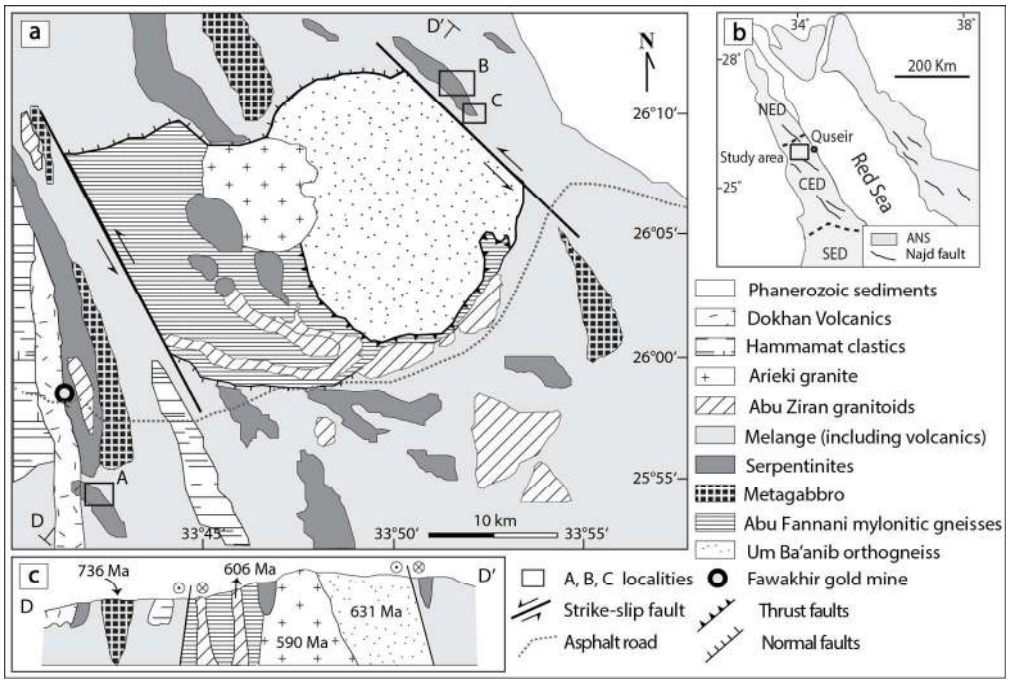

Figure 2. (a) General geological map of Neoproterozoic basement in the Meatiq area (after El-Gaby et al. 1984; Loizenbauer et al. 2001; Andresen et al. 2009, 2010; Abd El-Rahman et al. 2010), showing important lithologies, sample localities and strike-slip structures. (b) Inset shows the location of the Meatiq area in the CED, Egypt. (c) Schematic cross-section across Meatiq Gneiss Dome showing the relationship between the Meatiq Dome lithologies, the surrounding ophiolitic rocks, Hammamat clastics and Dokhan Volcanics. The ages are from Andresen et al. (2009).

144x97mm (300 x 300 DPI)

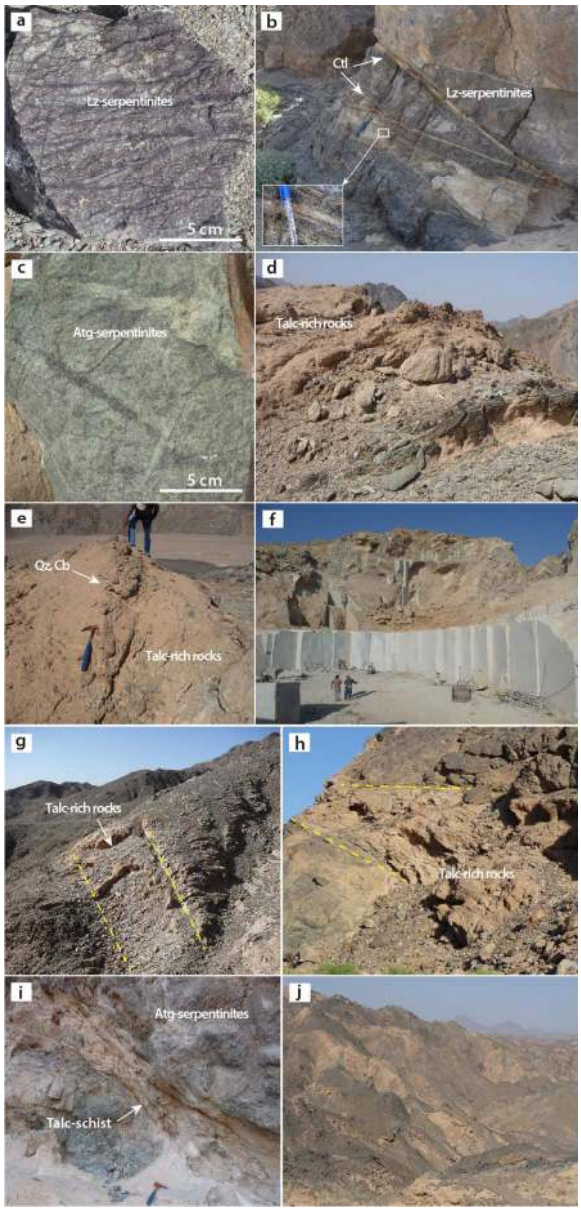

Figure 3. Field photographs of serpentinites and talc-rich rocks in the study area. (a) Mesh-textured Lz-serpentinite from locality A with visible chrysotile veinlets. (b) Lz-serpentinite exposures in locality A showing cross-cutting veinlets of fibrous chrysotile (Ctl). (c) Atg-serpentinite showing relict mesh textures from locality B. (d) Exposures of altered Atg-serpentinite from locality B. The pale layers are highly sheared talc-rich rocks. Location of photo is shown in Figure 4. (e) A carbonate (Cb) and quartz (Qz) vein hosted within sheared talc-rich rocks from locality B. Location of photo is shown in Figure 4. (f) The talc quarry from locality B showing cut surfaces of Atg-serpentinite. Location of photo is shown in Figure 4 (g) talc-rich rocks in a shear zone with sharp contacts to altered serpentinites in locality C. (h) An exposure of serpentinite with pale coloured shear-hosted talc-rich rocks from locality C. Sharp contact with shear zone to altered serpentinite control the location of the talc-rich rocks. (i) Sheared talc-schist between more coherent bodies of Atg-serpentinite from Locality C. (j) The view north from locality C showing extensive outcrop of shear-hosted listvenitic rocks within serpentinite.

139x292mm (150 x 150 DPI)

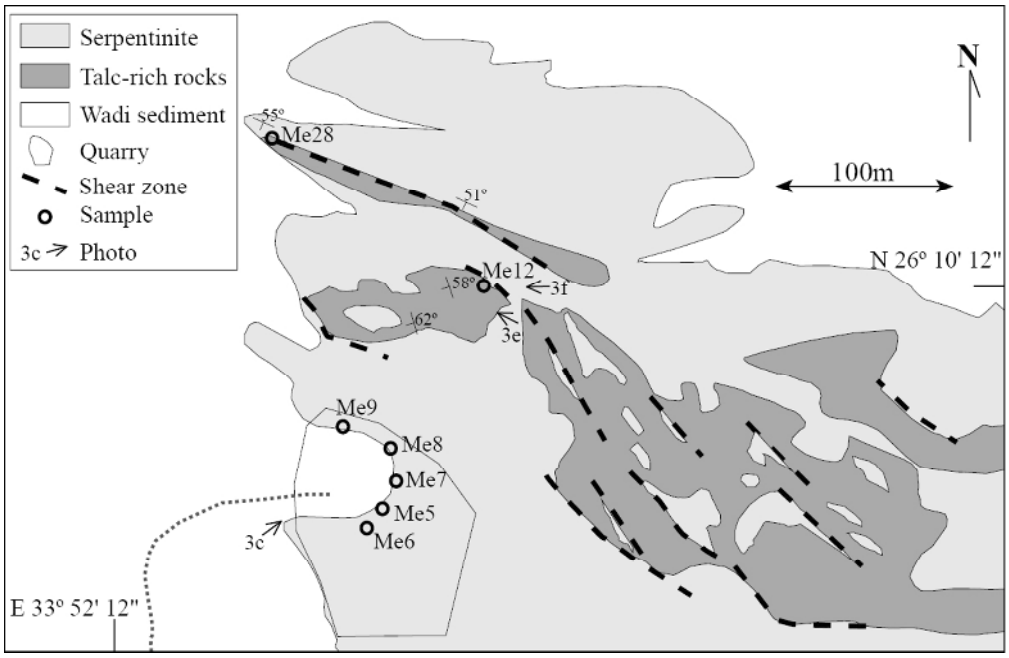

Figure 4. Simplified geological map of locality B showing patches of talc-rich rocks within antigorite serpentinite, the location of the talc quarry, sampling localities, and the position where photos in figure 3 were taken. The dotted line leading to the quarry is a road.

100x65mm (300 x 300 DPI)

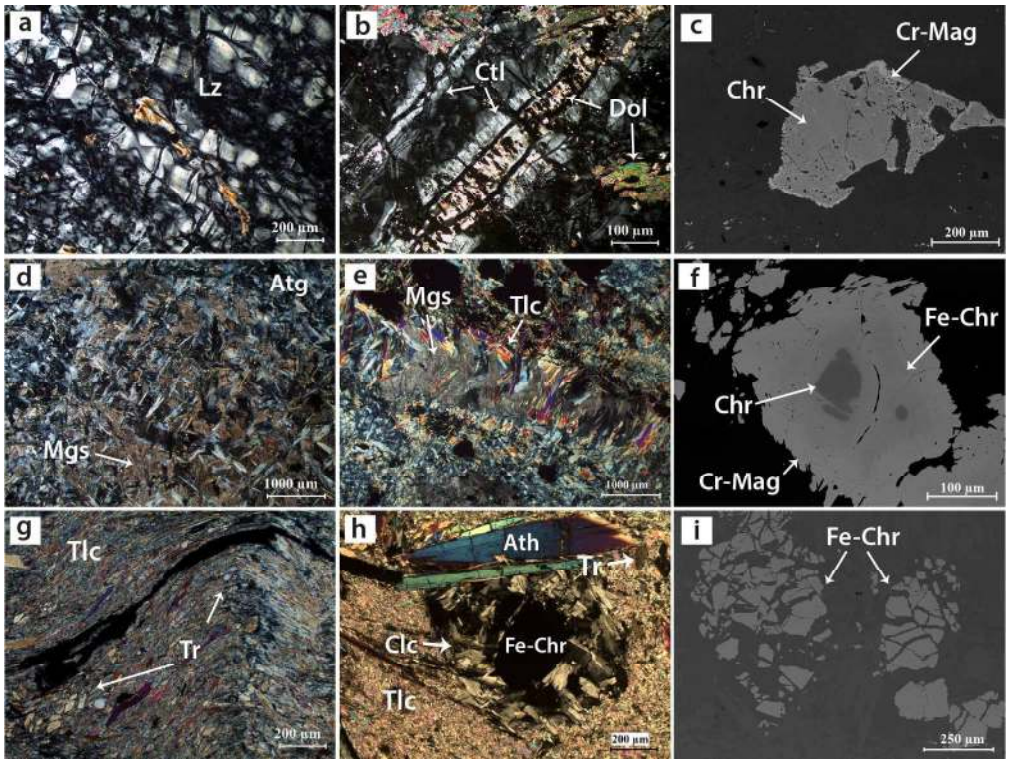

Figure 5. Photomicrographs (a, b, d, e, g, h) and back-scattered electron (BSE) images (c, f and i) of the investigated ophiolitic rocks in Meatiq area. (a) Lz-serpentinite with mesh texture and lizardite hourglass pseudomorphs after olivine together with late chrysotile veinlets, locality A-sample Me21. (b) Late chrysotile (Ctl) veinlets invaded by diffusive dolomite (Dol), locality A-sample Me22. (c) Slightly altered Cr-spinel with a very thin narrow Cr-rich magnetite (Cr-Mag) rim, locality A-sample Me21. (d) Antigorite flakes are intergrown with magnesite (Mgs) and minor talc (Tlc) in Atg-serpentinite, locality B-sample Me5. (e) Atg-serpentinite invaded by vein of talc and magnesite, locality B-sample Me9. (f) Cr-spinel alteration to ferritchromite (Fe-Chr) and Cr-rich magnetite (light-grey) with preservation of unaltered chromite (Chr, dark-grey) in the core, locality B-sample Me5. (g) Dynamically crystallized tremolite (Tr) in highly foliated talc-schist during progressive deformation, locality C-sample Me15. (h) Talc-schist rock with long anthophyllite fibres and ferritchromite embedded in chromium clinochlore (Clc), locality C-sample Me17. (i) Cataclastic texture in altered Cr-spinel (Fe-Chr) grain indicates intensive shearing in fault zones locality C-sample Me1.

163x123mm (300 x 300 DPI)

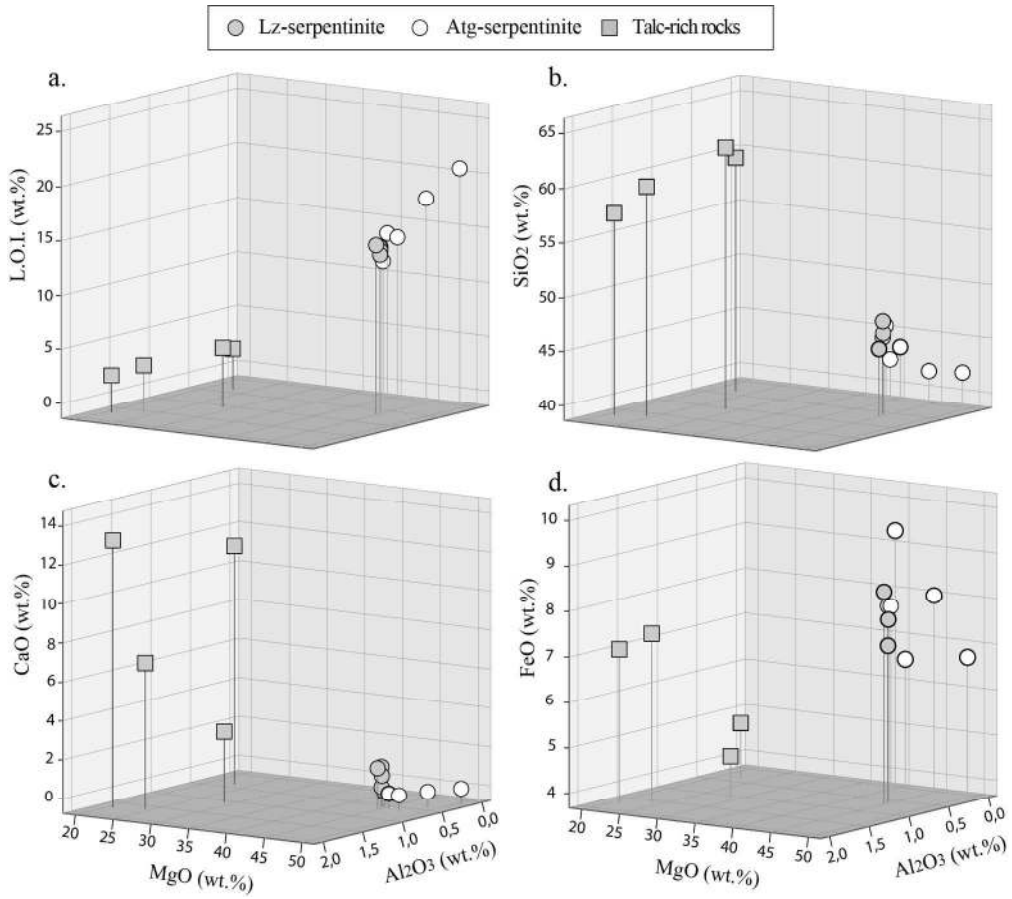

Figure 6. Three-dimensional representation of LOI and major elements, showing their distribution in two varieties of serpentinites and talc-rich rocks in the study area. Compositions are recalculated on a volatile free basis.

168x150mm (300 x 300 DPI)

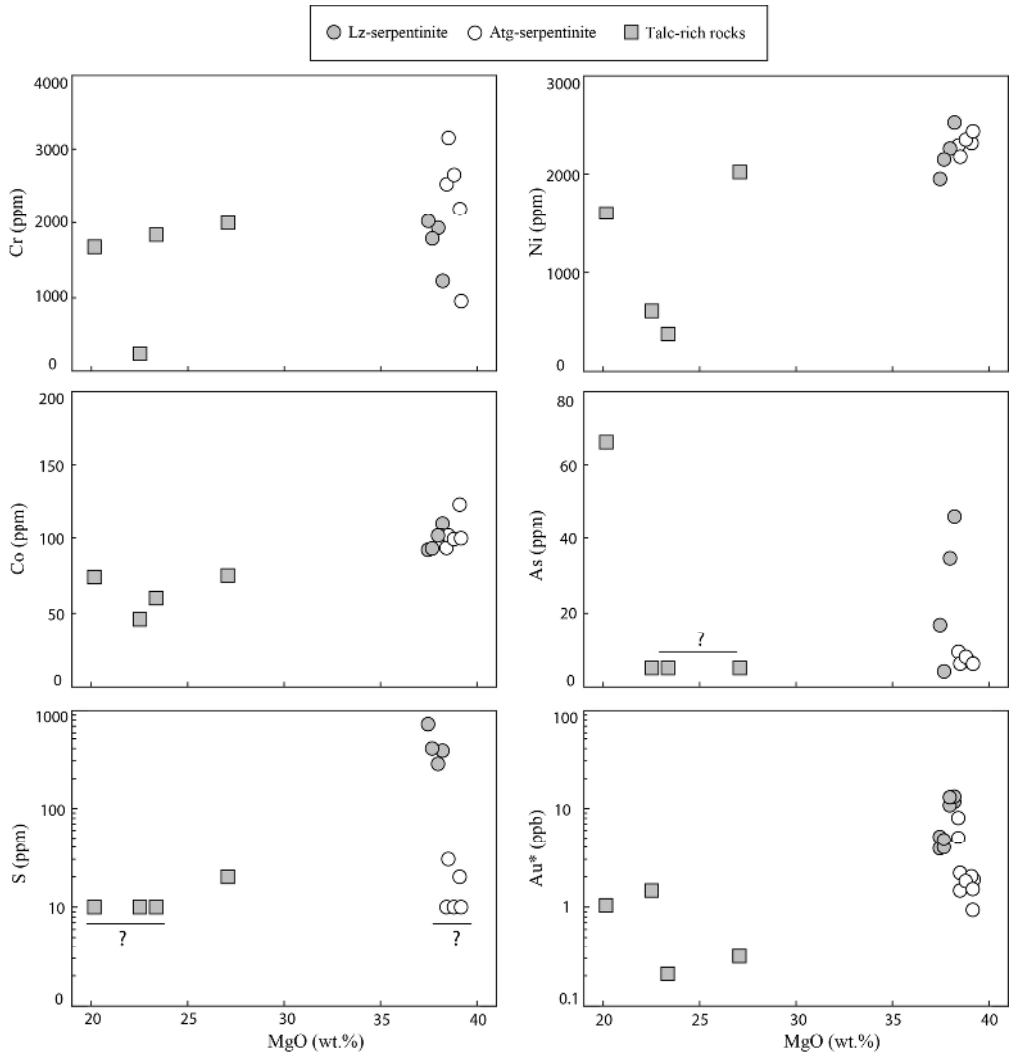

Figure 7. Harker-type diagrams showing variations in compatible trace elements of different serpentinites and talc-rich rocks. Au values plotted from two sets of serpentinites analyses. Question marks indicate values below detection limit.

157x164mm (300 x 300 DPI)

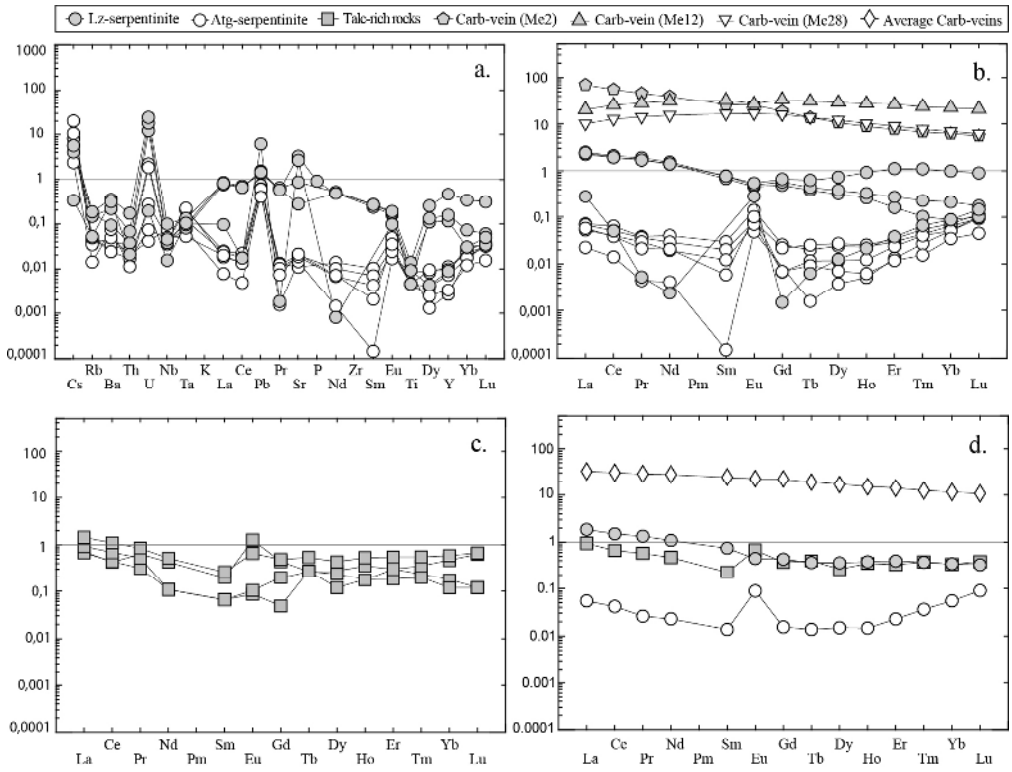

Figure 8. Trace element patterns for two varieties of serpentinites, talc-rich rocks and carbonate veins. (a) Compositions of Lz- and Atg-serpentinites. Primitive mantle normalizing values are after McDonough and Sun (1995). (b) and (c) REE compositions of two varieties of serpentinites, carbonate veins, and talc-rich rocks, respectively. (d) Average compositions of Lz- and Atg-serpentinites, talc-rich rocks and carbonate veins. Chondrite-normalizing values after McDonough and Sun (1995).

141x107mm (300 x 300 DPI)

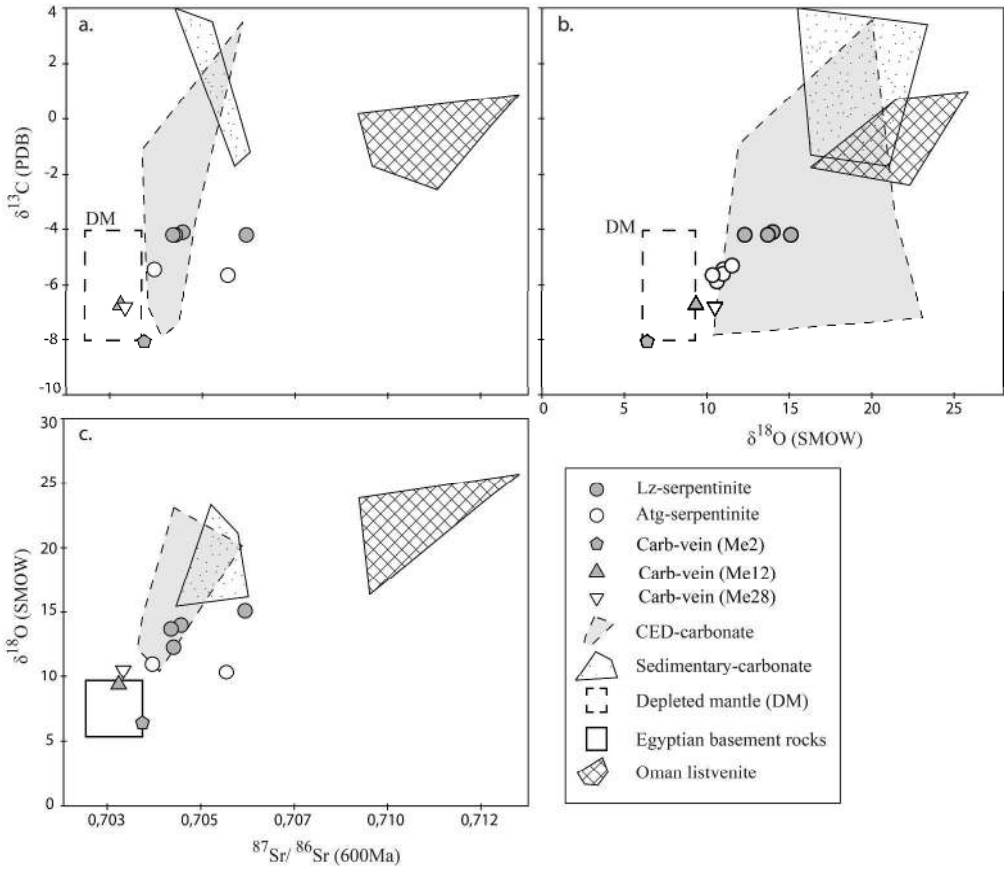

Figure 9. Plots of O, C and Sr isotope data for Meatiq serpentinites and carbonate veins. Data for Central Eastern Desert (CED) and sedimentary carbonates are adopted from Stern and Gwinn (1990). Field of Neoproterozoic mantle-derived carbonates (dashed-line boxes) is taken from C-isotopic data of Taylor et al. (1967) and Deines (1989), and Sr-isotopic data for Egyptian basement rocks (solid-line box) is from Stern and Hedge (1985). Data for Oman listvenites are adopted from Falk and Kelemen (2015). (a) δ13C vs. 87Sr/86Sr at ~ 600Ma; (b) δ13C vs. δ18O from the same samples, with similar fields displayed; (c) δ18O vs. 87Sr/86Sr at ~ 600Ma with similar reference fields outlined.

128x110mm (600 x 600 DPI)

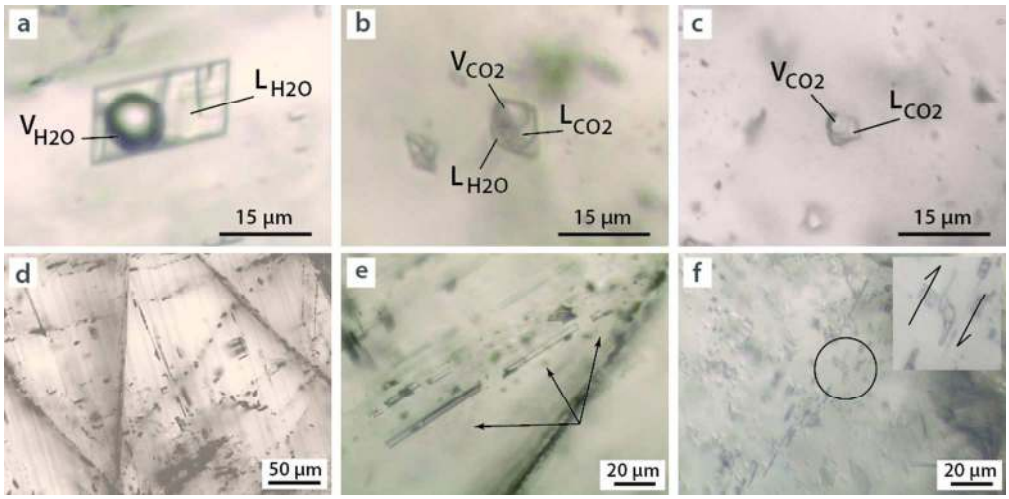

Figure 10. Photomicrographs of typical fluid inclusions in quartz/carbonate veins: (a) type-I, aqueous inclusion (LH2O+VH2O). (b) Type-II, aqueous-carbonic (LH2O+LCO2+VCO2). (c) Type-III, carbonic inclusion (LCO2+VCO2). (d) Trails of secondary inclusion crossing grain boundaries. (e) Elongation and necking down of inclusions in the direction of the trails. (f) Fluid inclusion with shear sense in magnesite vein (Me9).

178x87mm (150 x 150 DPI)

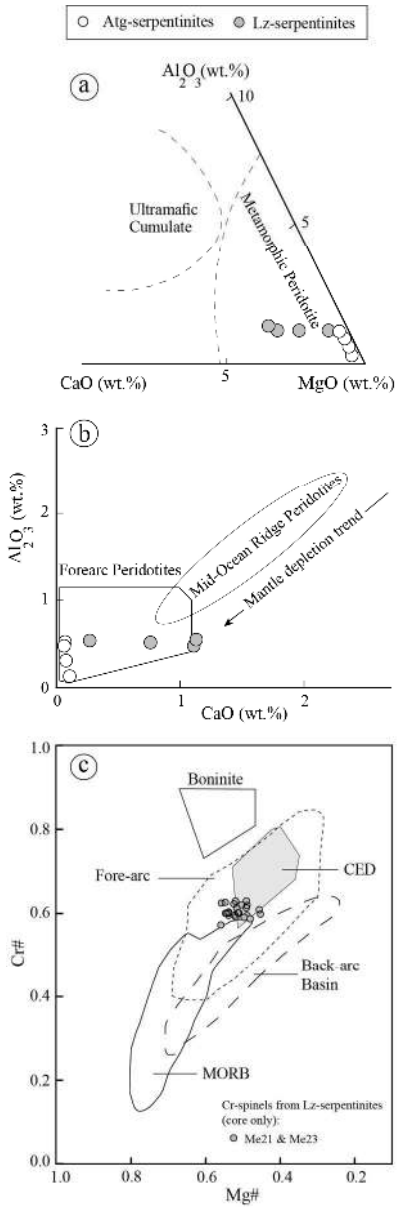

Figure 11. (a) Ternary plot of Al2O3-MgO-CaO for bulk rock compositions of Meatiq serpentinites compared with peridotites from other tectonic settings (after Coleman 1977). (b) CaO vs. Al2O3 diagram comparing Meatiq serpentinites with peridotites from other tectonic settings (after Ishii et al. 1992). (c) Cr# versus Mg# for the analyzed spinel cores in Meatiq serpentinites. Data for different tectonic environments were compiled from the literature following Stern et al. (2004). The field for core of Cr-spinel compositions occurring in some of the serpentinites from the Central Eastern Desert of Egypt (CED) is also shown (Azer and Stern 2007; Hamdy et al. 2013; Azer 2014). MORB = mid-ocean ridge basalt. Compositions are recalculated on a volatile free basis.

79x236mm (300 x 300 DPI)

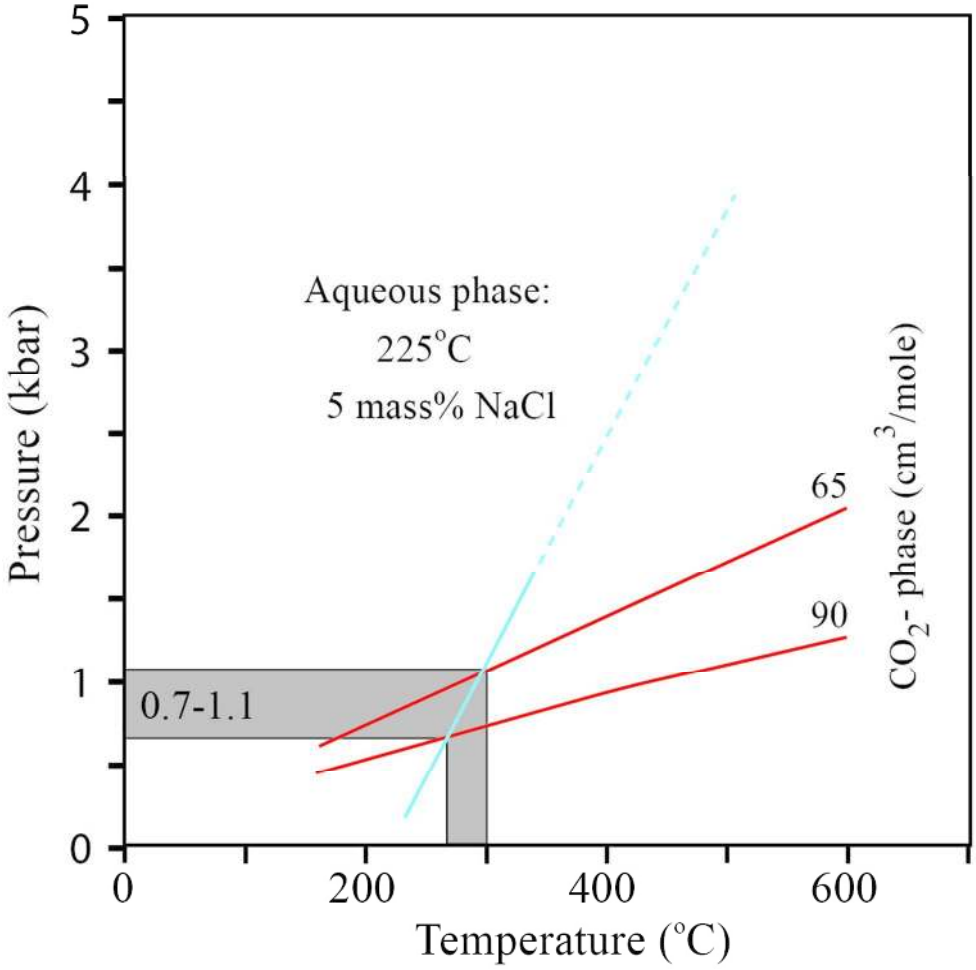

Figure 12. P-T diagram based on intersecting isochores of aqueous fluid inclusions with homogenization of 225°C and a salinity of 5 mass% NaCl and CO2 inclusions with molar volumes of 65 and 90 cm3/mol. The diagram shows estimated trapping condition for fluid inclusions in carbonate veins at 270°C-300°C and 0.7-1.1 kbar.

103x102mm (300 x 300 DPI)

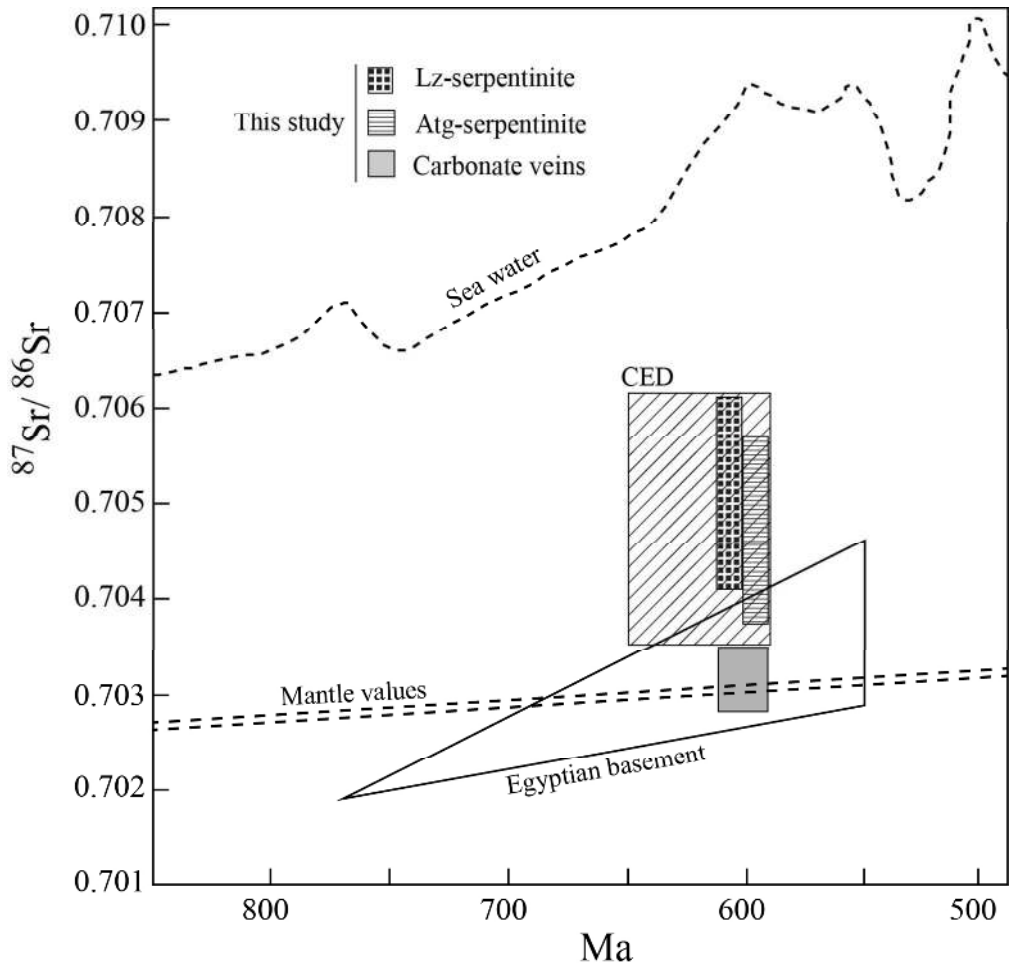

Figure 13. Sr composition of carbonate veins and altered serpentinites in the Meatiq study area compared to values from Neoproterozoic intrusive carbonates from Eastern Desert of Egypt. The ages of emplacement for the intrusive carbonates are estimated from the age of the surrounding basement units (after Cavanagh 1979; Stern and Hedge 1985; Reischmann 1986; Stern and Gwinn 1990). Field of initial 87Sr/86Sr for Egyptian basement igneous rocks is shown after Stern and Hedge (1985); this field represents an upper limit for the isotopic composition of Sr in the depleted mantle beneath northeast Africa at that time. Fields of initial 87Sr/86Sr for CED carbonate veins is shown after Stern and Gwinn (1990). Isotopic composition of Neoproterozoic seawater is also shown after Halverson et al. (2007).

133x128mm (300 x 300 DPI)

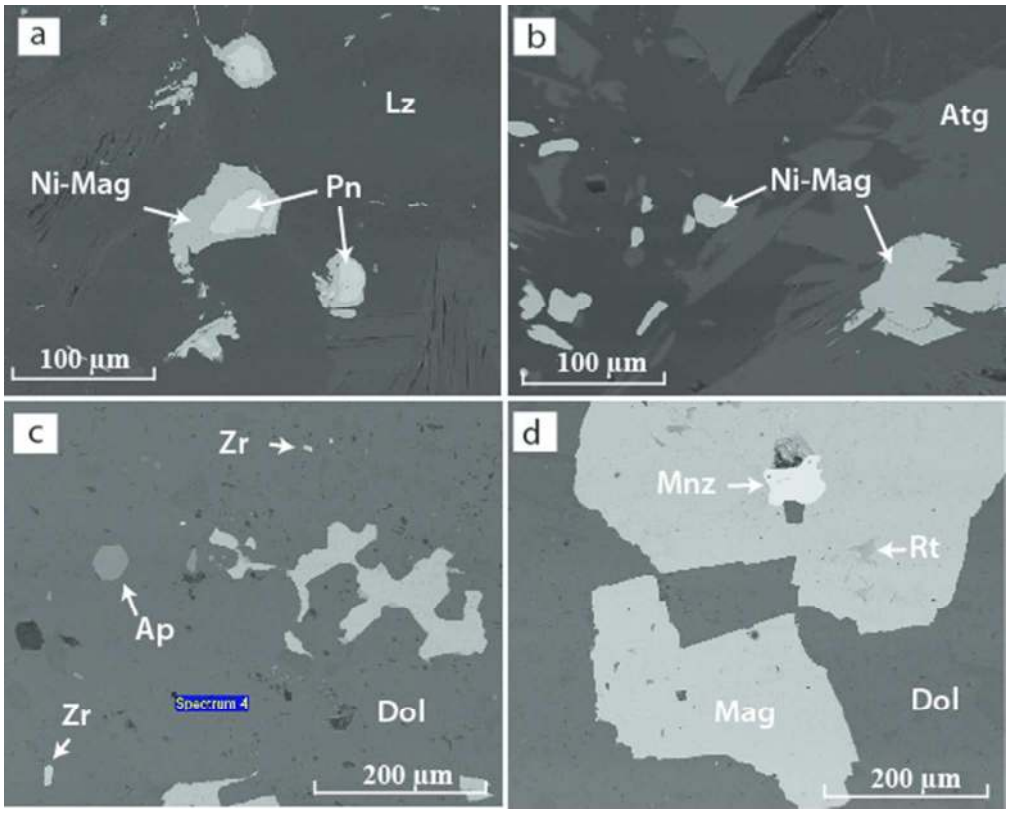

Figure 14. Back-scattered electron (BSE) images showing different mineral phases in serpentinites and carbonate veins. (a) Ni-sulphide (i.e. pentlandite-Pn) in Lz-serpentinites converted to Ni-rich magnetite (Ni-Mag) in the rims (Me23). (b) Total conversion of pentlandite to Ni-rich magnetite in Atg-serpentinites (Me7). Figures (c) and (d) show REE-bearing minerals (Zircon-Zr, apatite-Ap, Monazite-Mnz and rutile-Rt) in a carbonate vein (Me12).

98x79mm (150 x 150 DPI)

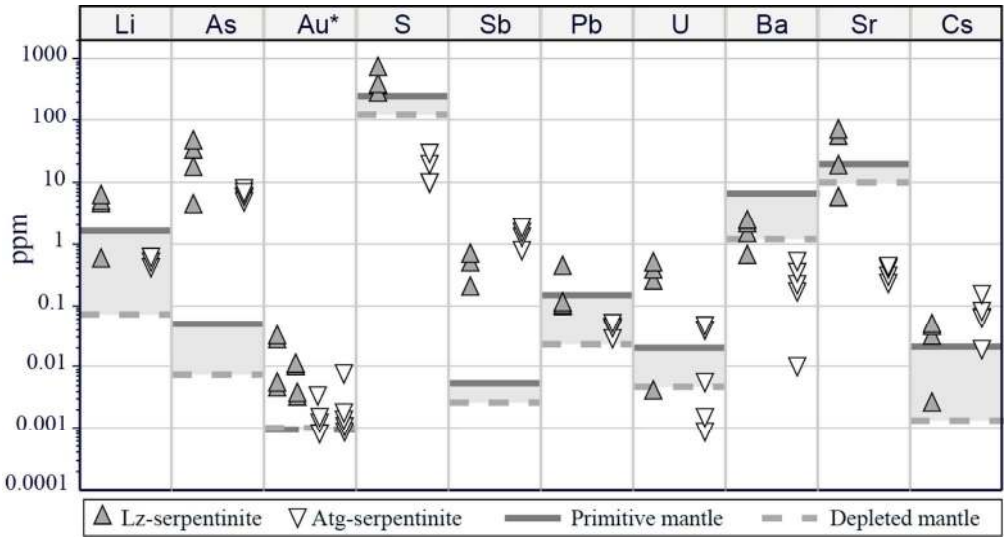

Figure 15. Plots of concentrations of fluid-mobile elements (Li, As, S, Sb, Pb, U, Ba, Sr and Cs) and Au in two serpentine phases from the Meatiq study area. Values of primitive mantle after McDonough and Sun (1995) and depleted mantle after Salters and Stracke (2004) are also reported (thick and dashed black lines). Grey boxes represent the ranges between primitive and depleted mantle. Au values plotted from two sets of serpentinites analyses.

106x56mm (300 x 300 DPI)

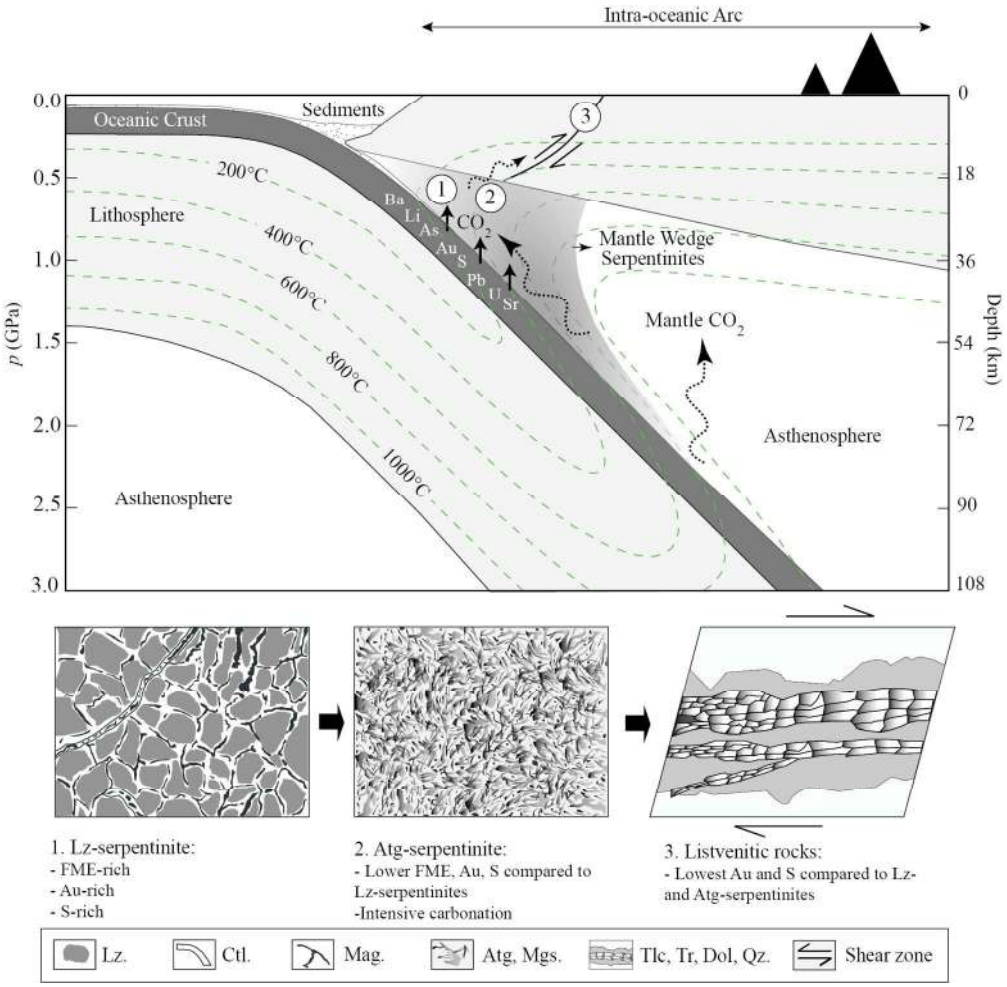

Figure 16. Schematic cross section illustrating the characteristics and evolution of the different serpentinite and listvenitic rocks and the tectonic setting where, based on the alteration assemblages and fluid inclusion compositions, these rocks formed. The principal transfer of fluid-mobile elements is also noted, as well as geochemical signature of fluids released during dehydration of serpentinites, "antigorite formation" due to the prograde metamorphism and later "listvenitization". Mineral abbreviations as in Fig. 5.

160x156mm (300 x 300 DPI)

Supplementary Table Representative electron microprobe analyses of Cr-spinel cores in Meatiq Lz-serpentinites

Sample No.	Me21										Me23													
Spot No.	1	2	3	4	5	6	7	8	9	10	1	2	3	4	5	6	7	8	9	10	11	12	13	14
TiO_2	n.d.	n.d.	0.013	0.012	n.d.	n.d.	n.d.	0.010	0.022	0.015	0.008	0.018	n.d.	n.d.	n.d.	n.d.	n.d.	n.d.	0.024	n.d.	n.d.	n.d.	n.d.	n.d.
Al_2O_3	20.08	21.10	20.55	19.83	19.86	20.68	21.78	19.94	19.76	19.77	21.87	21.20	21.04	21.55	21.88	21.49	21.74	23.03	21.11	21.20	21.17	21.24	21.38	20.78
Cr_2O_3	50.78	47.89	49.63	49.91	50.12	49.81	48.74	49.50	50.39	50.95	47.59	48.21	48.63	49.29	48.85	49.09	47.91	47.34	47.57	48.81	48.59	48.93	48.79	48.98
Fe_2O_3	0.387	1.203	0.703	0.978	0.804	0.715	0.677	0.794	0.860	0.548	0.884	0.799	0.895	0.264	0.488	0.616	0.695	1.052	1.575	0.956	0.737	0.957	0.556	0.488
FeO	17.24	19.29	19.35	18.84	18.00	18.38	17.76	19.23	16.81	18.28	19.78	20.70	18.48	17.75	18.48	17.74	18.29	17.13	19.05	17.47	18.58	17.30	18.63	20.53
MnO	0.178	0.195	0.219	0.095	0.160	0.284	0.172	0.120	0.074	0.189	0.200	0.266	0.130	0.113	0.082	0.170	0.156	0.117	0.147	0.105	0.213	0.212	0.150	0.261
NiO	0.052	0.098	0.031	n.d.	0.033	0.117	0.081	0.085	0.098	0.035	0.025	n.d.	0.065	0.042	0.023	0.040	0.040	0.083	0.110	0.102	0.031	0.127	0.062	n.d.
MgO	11.70	10.36	10.48	10.71	11.14	11.03	11.60	10.32	11.89	11.10	10.27	9.620	10.96	11.61	11.30	11.60	11.10	12.20	10.55	11.65	10.88	11.72	10.96	9.66
Total	100.42	100.13	100.97	100.38	100.11	101.01	100.81	99.99	99.90	100.88	100.63	100.81	100.20	100.62	101.10	100.74	99.94	100.96	100.14	100.29	100.20	100.48	100.53	100.70
No. of cations on the basis of four oxygen atoms																								
Ti	n.d.	n.d.	0.000	0.000	n.d.	n.d.	n.d.	0.000	0.001	0.000	0.000	0.000	n.d.	n.d.	n.d.	n.d.	n.d.	n.d.	0.001	n.d.	n.d.	n.d.	n.d.	n.d.
Al	0.738	0.782	0.757	0.735	0.736	0.758	0.793	0.743	0.730	0.728	0.804	0.784	0.776	0.787	0.796	0.784	0.800	0.831	0.781	0.777	0.781	0.777	0.785	0.770
Cr	1.253	1.190	1.226	1.241	1.245	1.225	1.191	1.238	1.249	1.258	1.174	1.196	1.203	1.207	1.192	1.202	1.183	1.145	1.181	1.200	1.202	1.201	1.202	1.218
Fe^{3+}	0.009	0.028	0.017	0.023	0.019	0.017	0.016	0.019	0.020	0.013	0.021	0.019	0.021	0.006	0.011	0.014	0.016	0.024	0.037	0.022	0.017	0.022	0.013	0.012
Fe^{2+}	0.450	0.507	0.506	0.496	0.473	0.478	0.459	0.508	0.441	0.478	0.516	0.543	0.484	0.460	0.477	0.459	0.478	0.438	0.500	0.454	0.486	0.449	0.485	0.540
Mn	0.005	0.005	0.006	0.003	0.004	0.007	0.005	0.003	0.002	0.005	0.005	0.007	0.003	0.003	0.002	0.004	0.004	0.003	0.004	0.003	0.006	0.006	0.004	0.007
Ni	0.001	0.002	0.001	n.d.	0.001	0.003	0.002	0.002	0.002	0.001	0.001	n.d.	0.002	0.001	0.001	0.001	0.001	0.002	0.003	0.003	0.001	0.003	0.002	n.d.
Mg	0.544	0.485	0.488	0.502	0.522	0.512	0.534	0.486	0.556	0.517	0.478	0.450	0.511	0.536	0.520	0.535	0.517	0.557	0.494	0.540	0.507	0.542	0.509	0.453
Mg#	0.547	0.489	0.491	0.503	0.525	0.517	0.538	0.489	0.558	0.520	0.481	0.453	0.514	0.538	0.522	0.538	0.520	0.559	0.497	0.543	0.511	0.547	0.512	0.456
Cr#	0.626	0.595	0.613	0.621	0.623	0.613	0.595	0.619	0.625	0.629	0.587	0.598	0.602	0.604	0.596	0.601	0.592	0.573	0.591	0.600	0.601	0.600	0.601	0.609
Fe^{3+}#	0.005	0.014	0.008	0.012	0.010	0.008	0.008	0.009	0.010	0.006	0.010	0.009	0.011	0.003	0.006	0.007	0.008	0.012	0.019	0.011	0.009	0.011	0.007	0.006

Mg# = Mg/(Mg+Fe^{2+}), Cr# = Cr/(Cr+Al), Fe^{3+}# = Fe^{3+}/(Fe^{3+}+Cr+Al), n.d. (not detected).